Extension of Geometrical Shock Dynamics for blast waves propagation

Julien Ridoux, Nicolas Lardjane, Laurent Monasse, François Coulouvrat

Shock Waves manuscript No.
(will be inserted by the editor)

Extension of Geometrical Shock Dynamics for blast waves propagation

J. Ridoux · N. Lardjane · L. Monasse · F. Coulouvrat

Received: date / Accepted: date

Abstract The direct numerical simulation of blast waves (accidental or industrial explosions) is a challenging task due to the wide range of spatial and temporal scales involved. Moreover, in a real environment (topography, urban area . . .), the blast wave interacts with the geometrical obstacles resulting in reflection, diffraction and waves recombination phenomena. The shape of the front becomes complex, which limits the efficiency of simple empirical methods. This work aims at contributing to the development of a fast running method for blast waves propagation in presence of obstacles. This is achieved through an *ad-hoc* extension to the simplified hyperbolic Geometrical Shock Dynamics model for shock waves propagation. This leads to a drastic reduction of the computational cost, from the five three-dimensional Euler equations to a two-dimensional problem with two equations. The new model, called Geometrical Blast Dynamics (GBD), is able to take into account any type of source and interactions with obstacles. Results are compared on a wide range of configurations with experiments, semi-empirical models from the literature and Eulerian simulations. A noticeable restitution of the blast wave propagation is observed.

J. Ridoux · N. Lardjane

CEA, DAM, DIF, Arpajon F-91297, France.

E-mail: nicolas.lardjane@cea.fr

L. Monasse

Université Côte d'Azur, Inria, CNRS, LJAD, EPC COFFEE, Parc Valrose, 06108 Nice, France.

J. Ridoux · F. Coulouvrat

Institut Jean Le Rond d'Alembert, UMR 7190 CNRS, Sorbonne Université, Paris, France.

Keywords Blast waves · Geometrical Blast Dynamics · Geometrical Shock Dynamics · Fast running method · Lagrangian scheme

1 Introduction

A blast wave results from the sudden release of a finite amount of energy from an impulsive source. A precise prediction of airborne blast waves propagation is required in numerous applications such as the pyrotechnics industry, explosion hazards or noise annoyance among others. The direct numerical simulation of blast waves from the detonation neighborhood to long range propagation is a challenging task due to the wide range of spatial and temporal scales involved. Moreover, the blast wave propagation is affected by numerous physical conditions such as the source shape, the height of burst, the interaction with obstacles or topography as well as the atmospheric conditions. This results in numerous physical phenomena such as diffraction, regular reflection, Mach stem formation or waves recombination. The shape of the front becomes complex, which limits the efficiency of simple empirical methods restricted to basic configurations.

As examples of canonical cases, we can cite the use of free field abacus such as Kinney and Graham's ones [1], coupled with empirical reflection [2] or with numerical diffraction [3] coefficients. Other examples include the energy concentration factor [4] for predicting blast propagation in partially confined geometries, or empirical laws for Mach stem evolution [1, 5, 2, 6] in the case of shock reflection over the ground. More sophisticated methods exist for simple structures such as the image burst method [5] for multi-reflected shock waves or the ray tracing method [7] for diffraction around structures. An example of the coupling of these methods can be found in [3] for blast-wave mitigation by a prismatic blast wall. For more complex three-dimensional configurations, the FLASH (Fast Lethally Assessment for Structures and Humans) code [8], designed to rapidly estimate explosion effects in urban areas, compiles these different geometrical methods. However, all these semi-empirical models are limited to simple geometries and their extension to arbitrary three-dimensional configurations seems difficult. As an alternative way, Flood [9] proposed to solved full Euler equations over a rough mesh, and then to use a neuronal network to refine results. The neuronal network is coupled with a data base previously provided by fine simulations. However, few details are provided about this approach. Moreover, the far field propagation turns out challenging given the important numerical diffusion occurring for rough meshes. Consequently, the development of alternative simplified models able to describe precisely blast waves propagation in complex environment and over long ranges is required.

Geometrical Shock Dynamics (GSD) model [10, 11, 12] is identified as a good alternative model for blast

waves propagation. It is able to estimate at a moderate cost, but with a reasonable accuracy, the propagation of a shock interacting with geometrical elements. This model is based on the decomposition of the shock front into elementary ray tubes. Assuming small changes in the ray tube area and neglecting the influence of the post-shock flow on the shock itself, a simple relation can be established [13], linking the local curvature and the front velocity, known as the $A-M$ rule. It is well known that GSD is quite accurate for sustained shock propagation problems. It has been investigated by numerous authors in the past, including among others cases of converging flows [14, 15], propagation through nonuniform media [16], and outdoor propagation [17] . Nevertheless, the model suffers from an intrinsic limitation for the issue of shock diffraction over a convex wall. For sufficiently weak shocks, no solution of GSD model exists up to the wall above a given deflection angle. This is in contradiction with experimental studies [18] showing that the diffracted shock front should still exist at the wall, even for weak shocks and at large deflection angles. Theoretical approach of nonlinear acoustics indicate that weak shock diffraction is dependent on the overall waveform, this means is influenced by post-shock flow [**?**]. Some modifications of GSD model, such as its extension to post-shock flow [13], or a modified treatment of the wall condition [19], are able to recover the inflection point experimentally observed for strong shocks, but do not remove the restriction. The more recent Kinematic model [20, 21, 22] is no more efficient to remove this limitation [23]. Based on the original Oshima's idea [24, 25] of transverse flow along the shock, an *ad-hoc* modification of the $A-M$ relation for two-dimensional configurations has recently be proposed in [26]. The closure is designed to systematically remove the limitation of the model.

GSD model is quite accurate for sustained shock propagation problems, for which post-shock flow has little influence on the shock propagation. In such a problem, the source energy is indeed infinite and continuously supplies the shock front. Consequently, the shock propagation is only driven by the local changes of shock geometry. It is no longer the case for blast waves propagation with a finite source of energy. Taking into account post-shock effects in the $A-M$ relation yields an infinite sequence of Ordinary Differential Equations (ODE) with higher-order post-shock flow terms [13]. Truncation at zeroth-order corresponds to the original GSD model. The dynamical influence of post-shock flow over the shock front is introduced as of first-order truncation. Nevertheless, an analysis of flow non-uniformities effects for blast waves reveals the complexity of choosing the order of truncation [27].

The objective of this paper is to present a simple extension of the GSD model to blast waves, much simpler than the high-order extension of the post-shock flow. The new model, called GBD model (Geometrical Blast Dynamics), is based on a decoupling between the shock front geometrical changes and the blast effects in the $A - M$ relation. It consists in modeling the post-shock flow term with an empirical law for spherical charges. As previously proposed [26], GBD model also includes additional transverse flow effects designed to remove the limitation of GSD model for the case of a shock diffracting over a convex wall.

The present paper is organized as follows. First, section 2 recalls the phenomenology of blast waves and presents some semi-empirical models selected to evaluate GBD model. Secondly, the derivation of GSD model and its *ad-hoc* modification to incorporate transverse flow is reviewed in section 3. The simple extension of GSD to blast waves is then fully described in section 4. The two-dimensional axisymmetrical conservative Lagrangian scheme, designed to solve GBD model, is also briefly recalled in this section. In section 5, GBD model is evaluated for several cases of increasing complexity and compared to semi-empirical models, Eulerian simulations and experimental data. Finally, section 6 provides a conclusion and suggests ways for further improving.

2 Problem set up

A blast wave results from a sudden and local release of a finite amount of energy from an impulsive source. As a consequence, a shock wave develops in air with a dramatic reduction in its strength as it propagates from away the source. For the ideal case of a spherical source in free field, Figure 1 sketches the typical temporal pressure signal. The shock, characterized by the peak overpressure ΔP^+, reaches the observation point (a gauge for example) at time t_a, called arrival time. The shock is continuously overtaken by an unsteady rarefaction wave resulting in an alternation between positive phase, where the pressure is up to ambient pressure p_0, and negative phase where it is down to p_0. The positive phase is fully described in terms of t_a, ΔP^+, the positive phase duration t^+ and the positive phase impulse I^+. The negative phase duration t^-, the pic underpressure ΔP^- and the negative phase impulse I^- characterizes the negative phase. The negative phase is usually not considered for most considerations such that the load evaluation on structures.

2.1 Free field laws

For a spherical or hemispherical charge of TNT[1], the empirical Kinney's laws [1] provides an approximation for main characteristics of blast waves. In particular,

[1] TNT: Trinitrotoluene, $C_7H_5N_3O_6$.

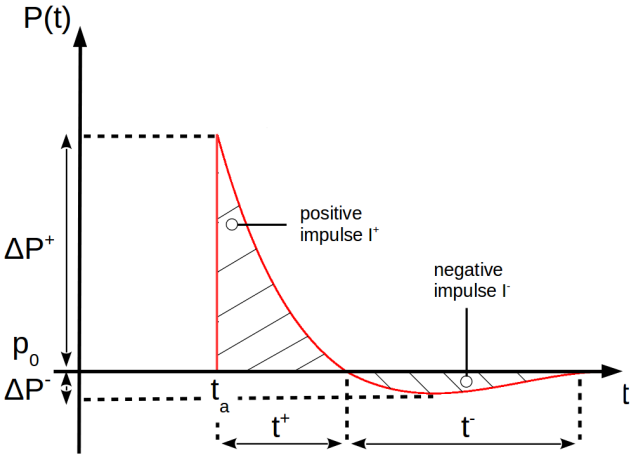

Fig. 1 Typical temporal pressure signal for an ideal blast wave according to [1].

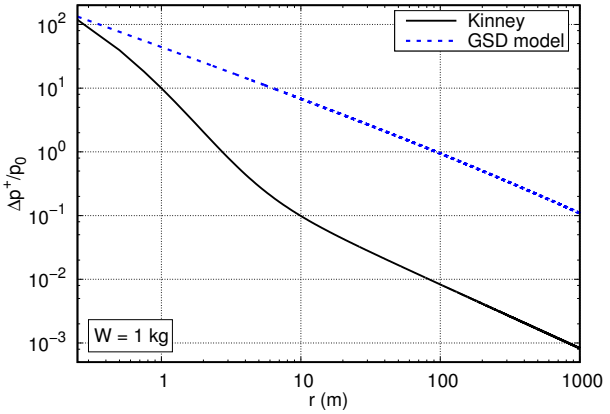

Fig. 2 Evolution of the peak overpressure in free field for the explosion of 1 kg of TNT from Kinney's law (1). GSD model is drawn as an indication. Results for GSD are obtained by solving (29) with a RK4 algorithm. The initial data are $r_0 = 0.25$ m and $M_0 \approx 10.124$, value calculated with (1) and (6).

the evolution of the non-dimensional peak overpressure, $\zeta_{\mathrm{K}} = \Delta p^+/p_0$, is expressed as

$$\zeta_{\mathrm{K}}(Z) = \frac{808\left(1+\left(\frac{Z}{4.5}\right)^2\right)}{\sqrt{\left(1+\left(\frac{Z}{0.048}\right)^2\right)\left(1+\left(\frac{Z}{0.32}\right)^2\right)\left(1+\left(\frac{Z}{1.35}\right)^2\right)}}, \quad (1)$$

where $Z = r/W^{1/3}$ is the scaled distance, r the distance at the source and W the mass of TNT expressed here in kilogram. The blast wave intensity, characterized by the peak overpressure, rapidly decreases with the distance as seen in figure 2. It degenerates to an acoustical wave, with an overpressure bellow to 20 mbar, at only 43 meters from the source. Another empirical laws for peak overpressure can be found in the literature, referred as Kingery's law [28] or the Needham's law [5] for example. In this paper, only Kinney's law is considered for condensed explosives. For another nature of explosive such that gaseous charges, let us cite the empirical law for a stoichiometric propane-oxygen mixture [3]:

$$\log\left(\zeta_{\mathrm{E}}(Y)\right) = 0.0895 - 1.7633\ln(Y) + 0.1528\ln(Y)^2 - 0.0066\ln(Y)^3 - 0.0021\ln(Y)^4, \quad (2)$$

with $\zeta_{\mathrm{E}} = \Delta p^+/p_0$, and where Y is the scaled distance reported to the released energy: $Y = r/E^{1/3}$ (in $\mathrm{m/MJ}^{1/3}$).

2.2 Blast wave reflection

Outdoor blast waves are affected by numerous physical conditions such as source shape, height of Burst (HoB) or interaction with obstacles. For a spherical explosion above the ground as sketched in figure 3, the shock wave interaction with the ground first results in a Regular Reflection (RR): incident and reflected shock waves are

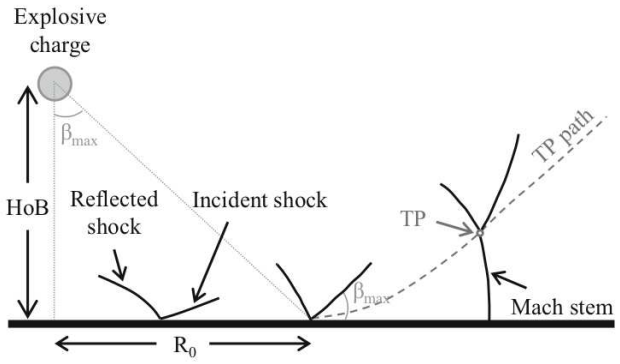

Fig. 3 Schematic representation of the interaction of an expanding spherical shock wave over the ground. Figure comes from [6].

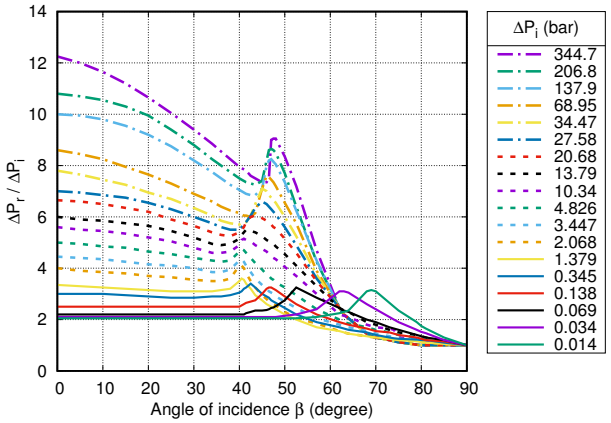

Fig. 4 Reflected pressure coefficients from UFC [2].

attached to the ground. From a distance at the ground R_0, depending on the shock intensity and the angle of incidence, both waves are unable to redirect the stream completely back into its original direction resulting in a Mach Reflection (MR). Incident and reflected shock waves are then detached from the surface and a third shock, called Mach stem, appears joining both waves to the ground at an intersecting point so-called Triple Point (TP). The Mach stem may be regarded as the fusion of the incident and reflected shock waves resulting in a rise of the peak overpressure [29]. The regime of reflection depends on past history of the shock and two main parameters [1]: the incident shock overpressure ΔP_i, or equivalently the incident Mach number M_i (6), and the angle of incidence β. The empirical Kinney's formula [1] provides an estimation of the critical angle of transition, β_max, between RR and MR:

$$\beta_\mathrm{max} = \frac{1.75}{M_\mathrm{i} - 1} + 39 \text{ (in degree)}. \tag{3}$$

Several empirical laws allows to estimating the distance of transition between RR and MR as well as the Height of Triple Point (HTP) [1, 2, 6, 30]. Boutillier *et al.* [6] defined an empirical law from experimental data for C4. The scaled ground distance, $SR_0 = R_0/W^{1/3}$, and the scaled height of burst, $SHTP = HTP/W^{1/3}$, are expressed for TNT as:

$$SR_0 = 1.99 \times 10^{-3} E_\mathrm{q}^{1/3} SHoB^2 + 0.601 SHoB, \tag{4}$$

$$SHTP = 0.07 \frac{SHoB}{SR_0^2} \left(SD^2 - 2SR_0 SD + SR_0^2\right), \tag{5}$$

where E_q is the TNT equivalency taken to 1.28 here. SD is the scaled distance at the ground: $SD = D/W^{1/3}$. These laws are valid for $SHOBs$ ranging from 22.7 cm/kg$^{1/3}$ to 159.7 cm/kg$^{1/3}$.

The reflected overpressure at the ground, ΔP_r, can be estimated with empirical reflection coefficients from UFC [2], shown in figure 4. This reflection table depends on β and ΔP_i, where ΔP_i can be evaluated with a free

field law such as Kinney's one (1). The reflection table intrinsically takes into account the regime of reflection.

2.3 Blast wave diffraction

In the case of diffraction of a spherical blast wave as sketched in figure 5(a), [3] proposes a numerical abacus inspired from reflection table (see figure 5(b)). This table gives the diffraction coefficient,

$$C_{\mathrm{d}} = \frac{\Delta P_{\mathrm{d}}}{\Delta P_{\mathrm{ff}}},$$

from the incident overpressure at the edge, ΔP_{i}, and the deflection angle $\theta_{\mathrm{w}} < 0$. The diffracted overpressure at the wall, ΔP_{d}, is then evaluated by multiplying C_{d} and the free field overpressure at the geometrical distance from the source to the observation point, ΔP_{ff}.

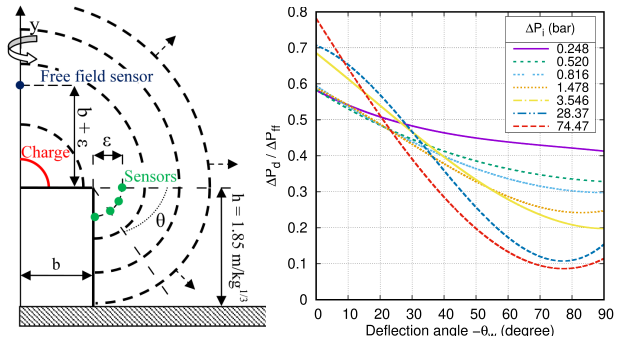

(a) (b)

Fig. 5 Configuration for blast wave diffraction over a convex corner (a) and diffracted pressure coefficients (b) from [3].

This abacus was established from numerical simulations in a 2D-axisymmetrical configuration for a structure with a deflection angle of $-90°$ and high of 1.85 m/kg$^{1/3}$ as sketched in figure 5(a). Sensors were located every $10°$ at $\epsilon = 0.015$ m/kg$^{1/3}$ from the corner and recorded the peak overpressure.

All empirical and semi-empirical laws are alternative approaches to the direct simulation of blast waves for simple geometries. Nevertheless, they are unable to estimate blast waves propagation in interaction with complex environment. An intermediate model, able to account for the shock interaction with structures of any shape, is the Geometrical Shock Dynamics model.

3 Review of GSD model

In this section, we recall the classical derivation of the Whitham's Geometrical Shock Dynamics (GSD) model [12]. Its limitation for expansive shock waves is discussed, followed by the presentation of a simple correction aiming at removing this restriction.

We consider the propagation of a shock wave in a uniform, quiescent, and calorically perfect gas. We denote by ρ, p, and v the density, pressure, and fluid velocity respectively. For a perfect gas, the sound speed c reads

$$c = \sqrt{\frac{\gamma p}{\rho}},$$

with γ the specific heat ratio of the gas, supposed constant and equals to 1.4 for air. These variables are in-

dexed by 0 for the initial state of the gas at rest. The standard conditions for air are $p_0 = 101,325$ Pa, that is $p_0 = 1.01325$ bar, $\rho_0 = 1.225$ kg/m^3 and $c_0 = 340.3$ m/s.

We introduce the shock Mach number:

$$M = \frac{U}{c_0} \geq 1,$$

where U denotes the shock velocity. The Rankine-Hugoniot relations [31] links this quantity to the shock overpressure ΔP^+:

$$M = \sqrt{1 + \frac{\gamma + 1}{2\gamma} \frac{\Delta P^+}{p_0}}. \tag{6}$$

The shock position, $\boldsymbol{x}$, is a solution of the Ordinary Differential Equation (ODE):

$$\frac{\mathrm{d}\boldsymbol{x}}{\mathrm{d}t} = U\boldsymbol{n} = c_0 M \boldsymbol{n}, \tag{7}$$

where t is the arrival time of the shock, and $\boldsymbol{n}$ denotes the unit outward normal vector at the front.

3.1 Geometrical Shock Dynamics model

The Whitham's GSD model is a simplified model for shock wave propagation based on a geometrical vision of the evolution of the shock front. The key idea behind GSD model consists in splitting the shock front into elementary areas, A, propagating along ray tubes in which the cross-flow is neglected. The model of shock propagation is thus reduced to the 1D problem of a planar shock moving into a channel with varying cross section.

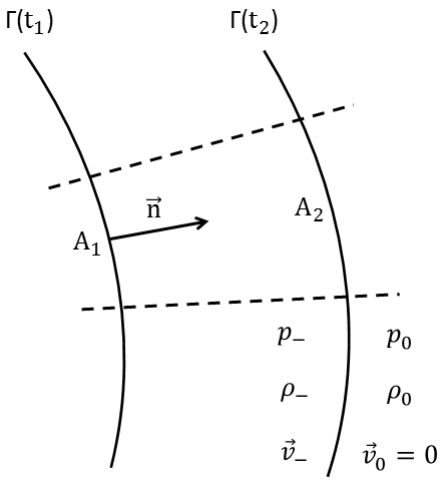

Fig. 6 Shock position at times t_1 and t_2. Quantities indexed by 0 are fluid parameters of the initial state of the gas, and quantities indexed by $-$ are fluid parameters disturbed by the shock.

At time t, the shock front is identified as the zero level set of a scalar function Φ :

$$\Gamma(t) = \{\boldsymbol{x} \in \Omega \subset \mathbb{R}^3 / \Phi(\boldsymbol{x}, t) = 0\}. \tag{8}$$

In the neighbourhood of the shock, we suppose that Φ is differentiable and that $\boldsymbol{\nabla}\Phi$ is not identically null. From (8), the unit normal vector at the shock front is defined by

$$\boldsymbol{n} = \frac{\boldsymbol{\nabla}\Phi}{|\boldsymbol{\nabla}\Phi|}, \tag{9}$$

and Φ verifies the equation:

$$\frac{\partial \Phi}{\partial t} + U\boldsymbol{n} \cdot \boldsymbol{\nabla}\Phi = 0. \tag{10}$$

Injecting (9) into (10), we get:

$$U = -\frac{\partial_t \Phi}{|\boldsymbol{\nabla}\Phi|}. \tag{11}$$

Assuming a single-pass front, the level-set function Φ may be defined as

$$\Phi(\boldsymbol{x}, t) = \alpha(\boldsymbol{x}) - c_0 t, \tag{12}$$

where α describes the shock position. Since c_0 is constant, $\alpha = c_0 t$ is also called a pseudo-time for the sake of simplicity. The unit normal vector at the shock front, (9), is then

$$\mathbf{n} = \frac{\boldsymbol{\nabla}\alpha}{|\boldsymbol{\nabla}\alpha|}, \tag{13}$$

and the normal velocity of the shock, (11), leads to the local eikonal equation, equivalent to (7):

$$M|\boldsymbol{\nabla}\alpha| = 1. \tag{14}$$

GSD model consists in splitting the shock front into elementary areas A propagating along ray tubes in which the cross-flow is neglected. The flow in a ray tube can be expressed mathematically by the equation [11]

$$\boldsymbol{\nabla}\cdot\left(\frac{\boldsymbol{n}}{A}\right) = 0. \tag{15}$$

By considering a ray tube as a channel with rigid walls, a simple law linking A to M closes the system. This relation, called $A - M$ rule, is obtained from the 1D Euler system with varying cross-section [13]:

$$\frac{1}{A}\frac{\mathrm{d}A}{\mathrm{d}\alpha} + \frac{M\lambda(M)}{M^2-1}\frac{\mathrm{d}M}{\mathrm{d}\alpha} + h(M)Q = 0, \tag{16}$$

where

$$\lambda(M) = \left(1 + \frac{2}{\gamma+1}\frac{1-\mu^2}{\mu}\right)\left(1 + 2\mu + \frac{1}{M^2}\right), \tag{17}$$

$$h(M) = \frac{\gamma+1}{2}\frac{\mu(\mu-1)}{M^2-1}, \tag{18}$$

and μ is the post-shock Mach number :

$$\mu = \sqrt{\frac{(\gamma-1)M^2+2}{2\gamma M^2 + 1 - \gamma}}. \tag{19}$$

$Q = \dfrac{(\partial_t p + \rho c \partial_t v)_-}{p_0 c_0^3}$, indexed by $-$ for quantities just behind the shock, contains all the post-shock flow terms. Q is an unknown of the problem. As

$$\lim_{M\to 1} h(M) = -0.6 \quad \text{and} \quad \lim_{M\to+\infty} h(M) = 0,$$

Whitham chose to neglect the term of truncation under the assumption of the smallness of post-shock effects Q, resulting in the simple form:

$$\frac{1}{A}\frac{\mathrm{d}A}{\mathrm{d}\alpha} + \frac{M\lambda(M)}{M^2-1}\frac{\mathrm{d}M}{\mathrm{d}\alpha} = 0. \tag{20}$$

This approximation appears to work remarkably well in a large number of configurations [12, 32, 23] where the post-shock effects have little influence on the shock propagation as for sustained shock. Finally, GSD model is composed of geometrical system (13)-(14)-(15) and the $A - M$ relation (20).

The function λ is a bounded increasing function, varying from 4 at $M = 1$ to

$$\lambda_\infty = 1 + \frac{2}{\gamma} + \sqrt{\frac{2\gamma}{\gamma-1}} \approx 5.074, \quad \text{for } \gamma = 1.4, \tag{21}$$

as $M \to +\infty$.

From (20), A depends only on M and can be consider as dimensionless:

$$A(M) = \exp\left(-\int_{M_0}^{M} \frac{m\lambda(m)}{m^2-1}\mathrm{d}m\right), \tag{22}$$

with M_0 a reference Mach number. It is straightforward to prove the hyperbolicity of GSD model provided that $A'(M) < 0$, which is verified as $\lambda(M) > 0$ and $M \geq 1$. Some waves may thus develop on the shock front. They are responsible for the modification of the intensity, shape, and orientation along with front evolution. In particular, discontinuities, called shock-shocks, appear. They correspond to the triple point position on the shock when a Mach stem arises. It is worth noting that Mach reflections systematically occur for compressive flows due to the geometrical vision of the shock wave. Nevertheless, for regular reflection conditions, it has been noticed that the Mach stem height is small enough to assimilate the reflection as regular [12]. In any event, considering the simplicity of the model, a good agreement with data can be observed as shown in [23].

In presence of an obstacle, wall boundaries coincide with rays in Whitham's theory. Consequently, the front is orthogonal to the wall. The hyperbolicity property of GSD insures taking into account of the shock interaction with structures.

3.2 Limitation of GSD model

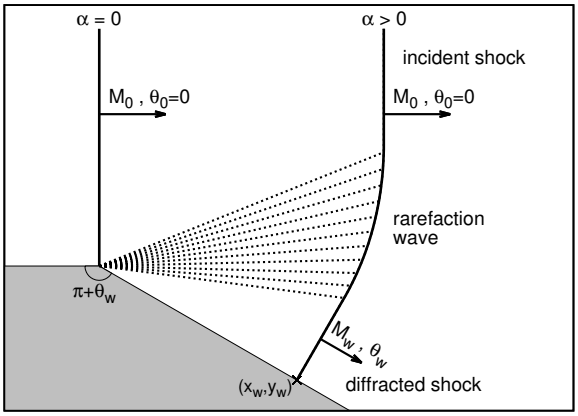

Fig. 7 Scheme of a planar shock diffraction over a convex corner in GSD theory. The solution is a rarefaction wave linking the initial state $(M_0, \theta_0 = 0)$ to the wall state $(M_\mathrm{w}, \theta_\mathrm{w})$.

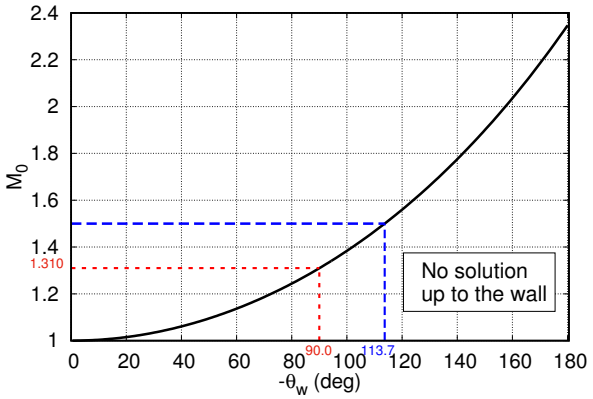

Fig. 8 Restriction curve (24) for a solution to exist for the diffraction of a planar shock over a convex wall. There is no solution up to the wall if (M_0, θ_w) is strictly below the curve. Two particular cases discussed in the text are indicated as examples by red and blue dotted lines.

As explained in [12, 26], the solution for GSD model is not insured for an expansive sufficiently weak shock. In 2D, this default is highlighted with the Riemann problem of a planar shock diffraction over a convex

wedge as sketched in figure 7. In this elementary problem, the shock travels from the left to the right at initial Mach number M_0, and diffracts over a convex wall of deflection angle $\theta_w < 0$ at time $\alpha = 0$. The first state for the Riemann problem is given by the incident shock: $(M_0, \theta_0 = 0)$. After diffraction, the wall Mach number, M_w, and the deflection angle, θ_w, represent the second state. It can be shown that a rarefaction wave links the states (M_0, θ_0) to (M_w, θ_w), diminishing the Mach number along the shock from M_0 to M_w. In particular, it results at the wall in [26]:

$$\int_{M_0}^{M_w} \sqrt{\frac{\lambda(m)}{m^2-1}}\mathrm{d}m = \theta_w - \theta_0 < 0. \tag{23}$$

From (23), one can easily show that a solution such that $M_w \geq 1$ exists if and only if $M_0 \geq M_{lim} > 1$, with M_{lim} the minimal reachable value of the incident Mach number:

$$\int_{1}^{M_{lim}} \sqrt{\frac{\lambda(m)}{m^2-1}}\mathrm{d}m = -\theta_w. \tag{24}$$

This means that, for a given incident Mach number M_0, no solution of GSD model exists up to the wall above a given deflection angle. Equivalently, for a given deflection angle $\theta_w < 0$, the condition $M_0 \geq M_{lim}$ must be verified to have a solution up to the wall.

The restriction (24) is plotted in figure 8. For any pair of variables (M_0, θ_w) in the area below the curve, there is no solution up to the wall for the diffraction of a planar shock over a convex corner. For instance, we have $M_{lim} \approx 1.310$ for $\theta_w = -90°$ and $M_{lim} = 1.5$ for $\theta_w \approx -113.7°$.

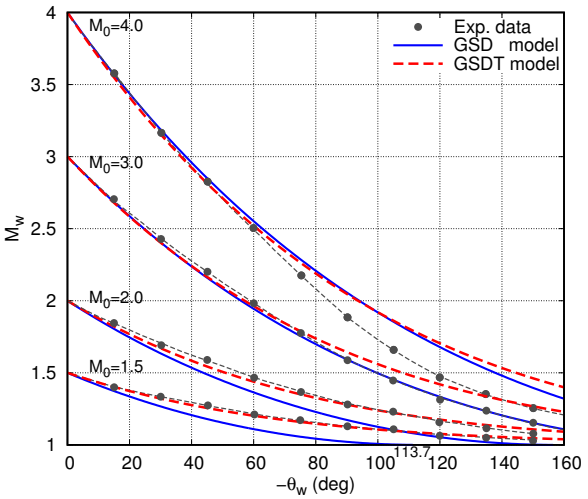

Fig. 9 Diffraction of a planar shock over a convex corner. Wall Mach number, M_w, with respect to deflection angle, θ_w in degrees, for different incident Mach numbers M_0. Comparison between Skew's experimental data [18] (black dots), GSD model (23) (black solid line), and GSDT model (25) (red dashed line).

The restriction of GSD model is in contradiction with Skew's experimental observations [18] as seen in figure 9. Indeed, experiments show that the diffracted shock front still exists at the wall, even for weak shocks ($M_0 = 1.2$) and at large deflection angles (θ_w up to $-165°$). Consequently, a modification of GSD is necessary.

3.3 *Ad-hoc* modification of the $A - M$ relation

More extensions of GSD model have been proposed taking into account the post-shock flow [13] or transverse

flow along the shock [24, 25] during the derivation of the $A-M$ relation. A modification of the treatment of the wall condition has been studied in [19]. However, all these modifications seem unable to completely remove the restriction. More recently, an *ad-hoc* correction of the $A-M$ rule (20), designed to systematically remove the limitation of the model, has been developed in [26]. In 2D, it consists on modelling the interaction between neighbouring ray tubes by the variation of the Mach number along the shock:

$$\frac{1}{A}\frac{\partial A}{\partial \alpha}+\frac{M\lambda(M)}{M^2-1}\frac{\partial M}{\partial \alpha}+H\left(\kappa\right)f(M)\left|\frac{\partial M}{\partial s}\right|=0, \qquad (25)$$

where s is the curvilinear abscissa along the shock. This modification is only active in expansive regions of the shock, namely region where the curvature of the shock curve, κ, is positive:

$$H(\kappa)=\begin{cases}0 & \text{if } \kappa\leq 0\\ 1 & \text{if } \kappa>0.\end{cases}$$

The function f is determined from an empirical law defined with Skews' experimental data [18]:

$$f(M)=\frac{k\lambda(M)}{2}-\frac{2M^2}{k(M^2-1)}, \quad k=0.985. \qquad (26)$$

The reader is referred to [26] for technical details. The system of geometrical equations (13)-(14)-(15) with the modified $A-M$ relation (25) is referred as GSDT, T standing for Transverse variation along the shock, in the remainder of the article.

Some studies in [26] have proven the ability of this new model to estimate in a better way the shock front position compared to GSD. In particular, GSDT model has a solution up to the wall for the problem of diffraction over a convex wedge as shown in figure 9.

GSDT model, without restriction for weak shocks contrary to GSD, is a good candidate to blast waves propagation extension. This point is developed in section 4.

3.4 Radial solutions for GSD and GSDT

For a planar ($d=1$), cylindrical ($d=2$) or spherical ($d=3$) shock wave, the evolution of the shock position (7) verifies the Ordinary Differential Equation (ODE):

$$\frac{\mathrm{d}r}{\mathrm{d}\alpha}=M(r). \qquad (27)$$

In this idealized configuration, the local variation of the area expresses in term of r and there is no transverse variation along the shock:

$$\frac{A'(r)}{A(r)}=\frac{d-1}{r} \quad \text{and} \quad \frac{\partial}{\partial s}\equiv 0. \qquad (28)$$

Consequently, GSDT model reduces in GSD model. From (20), the Mach number only depends on r:

$$M'(r)=-\frac{M^2(r)-1}{M(r)\lambda(M(r))}\frac{d-1}{r}. \qquad (29)$$

For a given initial condition $M(r_0)=M_0$, where r_0 is the initial shock position, the equation (29) can be

solved with a high-order algorithm. For example, figure 2 presents the solution obtained with a fourth-order Runge-Kutta scheme (RK4) with $r_0 = 0.25$ and $M_0 \approx 10.124$.

4 Simple extension of GSDT to blast waves and numerical integration

GSDT model are quite accurate for sustained shock propagation problems [26] for which the local changes of front curvature dominate post-shock effects. For blast waves, the modelling of post-shock contribution is necessary as seen in figure 2. In this section, a simple *ad-hoc* extension of GSDT model to blast waves is proposed for spherical or hemispherical charges.

4.1 Modelling of blast effects

Considering the post-shock flow in (25), the $A-M$ rule is expressed as

$$\frac{1}{A}\frac{\partial A}{\partial \alpha}+\frac{M\lambda(M)}{M^2-1}\frac{\partial M}{\partial \alpha}+H\left(\kappa\right)f(M)\left|\frac{\partial M}{\partial s}\right|+E=0, \quad (30)$$

with

$$E=h(M)\frac{(\partial_t p+\rho c\partial_t v)_-}{\rho_0 c_0^3},$$

where h is given by (18). We propose here to model E from an empirical law overpressure/distance at the source, r, available in free field for spherical or hemispherical charges. This law can be Kinney's law (1) for condensed explosives such as TNT, or a gaseous charge law (2) for a stoichiometric propane-oxygen mixture for example. Another modelling of the source may be possible.

Supposing E only depends on α, the shock Mach number variation in a ray tube results from a competition between geometrical effects, $\frac{1}{A}\frac{\partial A}{\partial \alpha}$, and blast effects, $E(\alpha)$: For a spherical shock wave ($d = 3$), the $A - M$ relation (30) becomes:

$$M\left(\frac{2}{r}+\frac{M\lambda(M)}{M^2-1}\frac{\mathrm{d}M}{\mathrm{d}r}\right)+E\left(\alpha\right)=0, \quad (31)$$

considering (27) and (28). For the sake of generality, let us denote $r \mapsto \zeta_{\mathrm{a}}(r)$ the law overpressure/distance. For example, we have $\zeta_{\mathrm{a}}(r) = \zeta_{\mathrm{K}}\left(r/W^{1/3}\right)$ for Kinney's law (1). From (6), the Mach number expressed as

$$M_{\mathrm{a}}(r)=\sqrt{1+\frac{\gamma+1}{2\gamma}\zeta_{\mathrm{a}}(r)}. \quad (32)$$

Injecting (32) into (31), the blast effects term may expressed as

$$E\left(\alpha\right)=E_{\mathrm{r}}(r_{\mathrm{a}}(\alpha)), \quad (33)$$

with

$$\frac{E_{\mathrm{r}}(r)}{M_{\mathrm{a}}\left(r\right)}=-\frac{2}{r}-\frac{\lambda\left(\sqrt{1+\frac{\gamma+1}{2\gamma}\zeta_{\mathrm{a}}(r)}\right)}{2}\frac{\zeta_{\mathrm{a}}'(r)}{\zeta_{\mathrm{a}}(r)}, \quad (34)$$

where $M \mapsto \lambda(M)$ is defined by (17). The mapping between α and r_{a} is expressed from the ODE (27), which results in the following integral form:

$$r_{\mathrm{a}}(\alpha)=r_0+\int_{\alpha_0}^{\alpha}M_{\mathrm{a}}(r_{\mathrm{a}}(\tau))\mathrm{d}\tau, \quad (35)$$

where r_0 is the shock position at initial time α_0. For a condensed explosive, the shock position at $\alpha_0 = 0$ corresponds to the charge radius:

$$r_0 = r_c = \left(\frac{3W}{4\pi\rho_c}\right)^{1/3}, \tag{36}$$

where ρ_c is the density of the explosive. For instance, $\rho_c = 1650$ kg/m^3 for TNT and $r_c = 0.053$ m for $W = 1$ kg. Finally, blast effects are modeled with relations (32)-(35) in relation (30).

The simplified model designed for blast waves propagation in presence of obstacles is finally composed of geometrical equations (13)-(14)-(15) and the *ad-hoc* $A-M$ relation (30). This model is referred as Geometrical Blast Dynamics (GBD) in the remainder of this article.

As discussed in section 3.1 for GSD model, GBD model naturally makes arise Mach stems for compressive flows. Consequently, GBD model does not taken into account the Regular Reflection. This point will be fully studied in section 5.

4.2 Analysis of the blast closure for TNT

In this section, the blast closure is analyzed for a spherical diverging blast wave issue from an explosion of a TNT charge. A similar analysis may be possible for a gaseous charge. The blast term, $E_r(r)/M_a(r)$, is modeled with Kinney's law (1). The dimensionless blast contribution (34) then depends only on the scaled distance $Z = r/W^{1/3}$:

$$\frac{E_r(r)}{M_a(r)} W^{1/3} Z_c = -\frac{2Z_c}{Z} - \frac{\lambda\left(\sqrt{1+\frac{\gamma+1}{2\gamma}\zeta_K(Z)}\right)}{2}\frac{\zeta_K'(Z)}{\zeta_K(Z)} Z_c, \tag{37}$$

where $Z_c \approx 0.053$ m/kg$^{1/3}$ is the scaled charge radius (36). From (1), one obtains:

$$\frac{\zeta_K'(Z)}{\zeta_K(Z)} = \frac{2}{Z\left(1+(4.5/Z)^2\right)} - \frac{1}{Z\left(1+(0.048/Z)^2\right)} - \frac{1}{Z\left(1+(0.32/Z)^2\right)} - \frac{1}{Z\left(1+(1.35/Z)^2\right)}. \tag{38}$$

In free field, the blast wave propagation results from a competition between the geometrical expansion,

$$\frac{A'(r)}{A(r)} W^{1/3} Z_c = \frac{2Z_c}{Z},$$

written as dimensionless, and the blast effects (37). Figure 10 draws each contribution versus the scaled distance.

Near field the source, the blast closure values are negative for $Z_c \leq Z \leq 0.079$ m/kg$^{1/3}$ and the geometrical expansion dominates up to $Z = 0.357$ m/kg$^{1/3}$. This observation results from the significant size of the explosive in Kinney's law (1), as $\zeta_K'(Z)/\zeta_K(Z) \propto Z$. Indeed, for the ideal case of a point source in the free field, the non-dimensional overpressure theoretically decreases as r^{-3} in the very near field [33]. This leads to $\zeta_a'(r)/\zeta_a(r) \propto r^{-1}$ and blast effects are proportional to Z^{-1}. Consequently, contributions of geometrical expansion and blast effects may be of the same order.

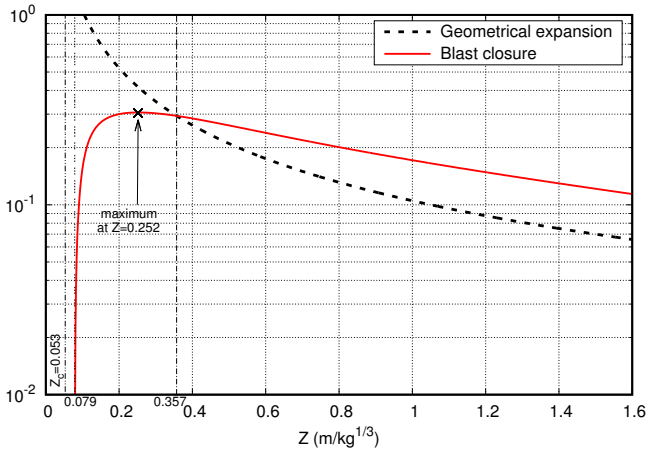

(a)

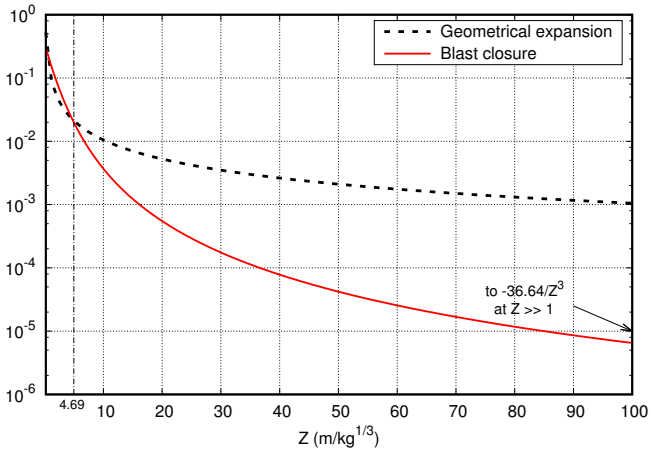

(b)

Fig. 10 Competition between the geometrical expansion, $\frac{A'(r)}{A(r)}W^{1/3}Z_{\rm c}$, and the blast effects, $\frac{E_{\rm r}(r)}{M_{\rm a}(r)}W^{1/3}Z_{\rm c}$, in GBD model (31) with Kinney's closure (1) for free field propagation up to 1.6 m (a) and 100 m (b) from the source.

For $Z \geq 0.1$ m/kg$^{1/3}$, both contributions are of the same order, which justifies and imposes to take into account the blast closure in the $A-M$ relation. The blast closure reaches a maximum at $Z \approx 0.252$ m/kg$^{1/3}$. Blast effects then decrease and dominate the geometrical expansion from 0.357 m/kg$^{1/3}$ to 4.69 m/kg$^{1/3}$.

The geometrical expansion takes precedent over blast effects as we go far from the source. At a 100 meters distance, an one hundred factor gap is observed. Although this contribution could be neglected at this distance, the modelling of blast effects appears necessary to keep the right decay of the shock intensity. For $Z \gg 1$, a Taylor expansion of (38) gives:

$$\frac{\zeta_{\rm K}'(Z)}{\zeta_{\rm K}(Z)} \sim -\frac{1}{Z} - \frac{C}{Z^3},$$

with $C = 4.5^2 - 0.048^2 - 0.32^2 - 1.35^2 \approx 18.32$ m^2/kg$^{2/3}$.

As $\lambda \sim 4$ for $M \sim 1$, the blast closure is expressed as:

$$\frac{E_{\rm r}(r)}{M_{\rm a}(r)}W^{1/3}Z_{\rm c} \sim \frac{2CZ_{\rm c}}{Z^3} > 0.$$

Consequently, blast effects contribution in the model keeps slowing down the shock front far field.

4.3 Numerical scheme

From the numerical point of view, a two-dimensional axisymmetrical conservative Lagrangian scheme has been developed and validated for GSDT model in [26]. The mean space step is denoted Δs. In the vicinity of a shock-shock, the transverse closure in (30) is deactivate for points at a distance $d_{\rm c}$ from the discontinuity for the sake of stability. The reader is referred to [26] for technical details.

The extension of the Lagrangian scheme to GBD model is direct. As proof of the validation for GBD closed with Kinney's law (1), the numerical solution in free field is compared with the analytical solution (1) in figure 11.

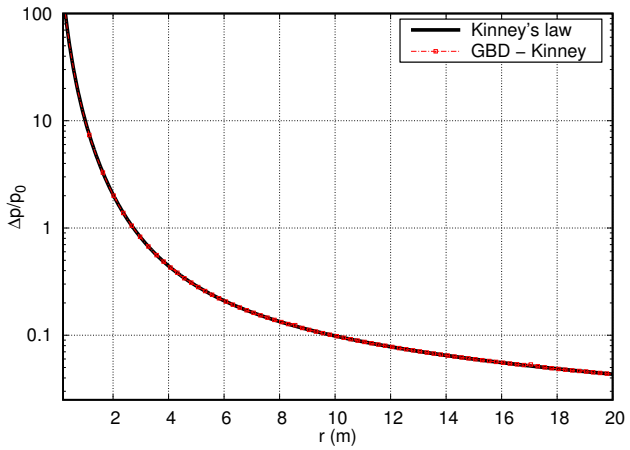

Fig. 11 Evolution of the peak overpressure in free field for the explosion of 1 kg of TNT from Kinney's law (1). The numerical solution is performed with $\Delta s = 0.01$. Initial data: $r_0 = 0.2$ and $M_0 \approx 11.70$.

5 Evaluation of GBD model

GBD model is now compared with semi-empirical models detailed in section 2, Eulerian simulations and experimental data on a wide range of configurations. Eulerian simulations are provided by the HERA Computational Fluid Dynamics software [36] which is a multi-physics code using adaptive mesh refinement (AMR).

GBD model is first evaluated on elementary configurations for a TNT charge: reflection over the ground, reflection over a concave corner and diffraction over a convex corner. For these evaluations, Kinney's law (1) closes GBD model as described in section 4.1. In the last subsection, GBD model is evaluated for a gaseous charge on a more complex problem combining both reflection and diffraction over surfaces: it is the interaction with a mound. For this case, GBD model is closed with the stoichiometric propane-oxygen mixture (2).

For mostly configurations, the error between GBD results and reference solutions are evaluated as

$$\text{error} = \frac{\text{GBD result} - \text{REF result}}{\text{REF result}} \times 100. \tag{39}$$

REF result refers to experimental data or semi-empirical model solutions.

For all cases, the resolution of GBD model is made with the Lagrangian scheme presented in section 4.3. The parameter d_c has been chosen after a parametric study for numerical solution convergence. Unless otherwise stated, the Lagrangian simulations have been performed with $\Delta s = 0.005$ and $d_c = 0.05$. Computational time takes a few minutes on a simple processor *Intel(R) Core(TM) i5-8300H CPU @ 2.30GHz.*

5.1 Reflection of a spherical blast wave over the ground

As a first example, we consider the explosion of a TNT charge at a Height of Burst, HoB, above the ground as sketched in figure 3. The spherical shock wave is first reflected over the ground in a regular way (RR: Regular Reflection): the incident and reflected shock waves are attached to the floor. From a distance at the ground R_0, the reflection then becomes irregular (MR: Mach Reflection). A Mach stem appears which joins the

incident and reflected shock waves at the Triple Point (TP). Here, Kinney's law (1) models blast effects in GBD model.

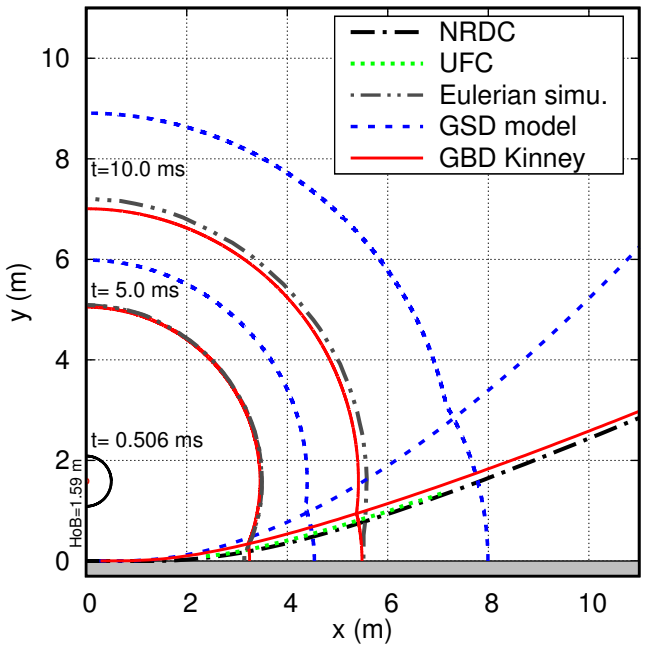

Fig. 12 Blast wave reflection over the ground generated by the explosion of 1 kg of TNT at a height of 1.59 m. Comparison between GSD, GBD with Kinney's closure, an Eulerian simulation and experimental data fits from NRDC [30] and UFC [2]. The Lagrangian simulations have been performed with $\Delta s = 0.005$ m and $d_c = 0.05$ m.

Figure 12 presents results for the explosion of 1 kg of TNT at a HoB of 1.59 meters. For this case, the transition between RR and MR arises around $R_0 = 1.48$ m at the ground according to (4). The shock positions at times 5 ms and 10 ms are compared with an Eulerian simulation. These ones are extracted from the simulation with a marching square algorithm [37] as explained in [23]. The shock-shock trajectory is compared with the TP path from experimental laws from literature. These last ones are taken from UFC [2], defined up to a distance of 7 meters, and NRDC [30]. In order to show the contribution of the blast closure, results are compared with GSD model. As expected, GSD model overestimates the shock positions as well as the TP path due to the truncation of post-shock flow. This discrepancy is drastically reduced with GBD model. One notes the correct prediction of the shock wave positions in comparison with the Eulerian simulation as well as the good restitution of the TP path with experimental laws.

Figure 13 shows a wider comparison of Triple Point trajectories between GBD model and experimental data from [6]. These data are issue from experiments for C4 and they are adapted here for TNT with TNT equivalency $E_q = 1.28$. Let us recall that $SHoB$, SD and $SHTP$ stand for the scaled HoB, the scaled distance at the ground and the scaled height of burst respectively:

$$SHoB = \frac{HoB}{W^{1/3}}, \quad SD = \frac{D}{W^{1/3}}, \quad SHTP = \frac{HTP}{W^{1/3}},$$

where W is the mass of TNT. For $SHoB \leq 113.6$

$SHoB$	23.6	45.1	68.5	85.0	113.6	132.9	166.2
SR_0	15.4	31.3	50.9	66.1	95.0	116.5	157.0

Table 1 Scaled distances of transition between RR and MR, SR_0 (in cm/kg$^{1/3}$), for several $SHoB$ (in cm/kg$^{1/3}$) according to (4).

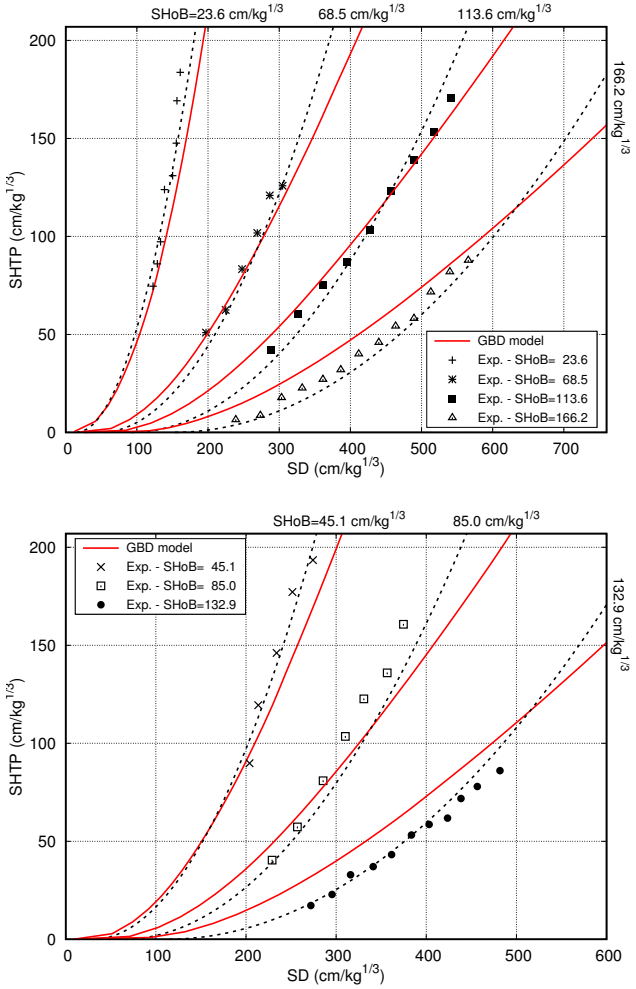

Fig. 13 Blast wave reflection over the ground generated by the explosion of TNT at a scaled height $SHoB = HoB/W^{1/3}$. Comparison of the TP paths between GBD with Kinney's closure and experimental data from [6]. The Lagrangian simulations have been performed with $\Delta s = 0.005$ m and $d_c = 0.05$ m. Dashed lines correspond to FIT (4)-(5) from [6].

cm/kg$^{1/3}$, GBD model is in excellent agreement with experiments. One notes a discrepancy with experimental data as $SHoB$ increases: the TP paths are overestimated by the model. This observation is a consequence of GBD to systematically produce a Mach stem for compressive flows as underlined in section 4.1. Actually, the reflection is regular up to a scaled distance SR_0 where a Mach Reflection arises. The table 1 lists this scaled distance for several $SHoB$ according to the empirical law (4). For small height of burst, the MR rapidly appears which justifies the excellent agreement of GBD model with experimental data. For larger $SHoBs$, the MR arises farther from the source. For example, for $SHoB = 132.9$ cm/kg$^{1/3}$, the reflection is regular up to around 116.5 cm. At this distance, GBD model provides a 2 cm high Mach stem, which affects its evolutionary and accordingly leads to the overestimation of the TP path.

5.2 Reflection of a spherical blast wave over a concave corner

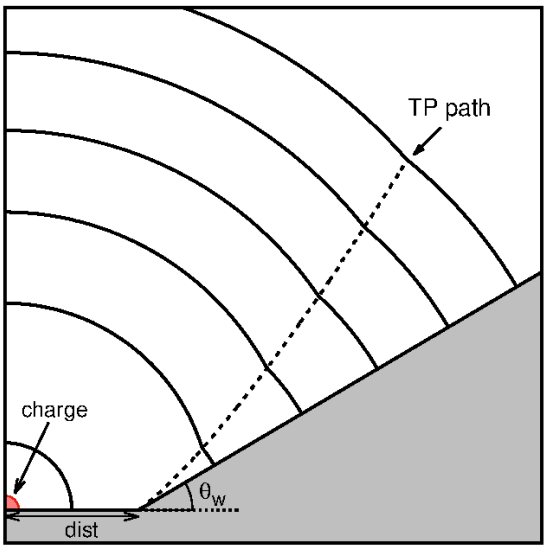

Fig. 14 Scheme a spherical blast wave reflection over a concave corner.

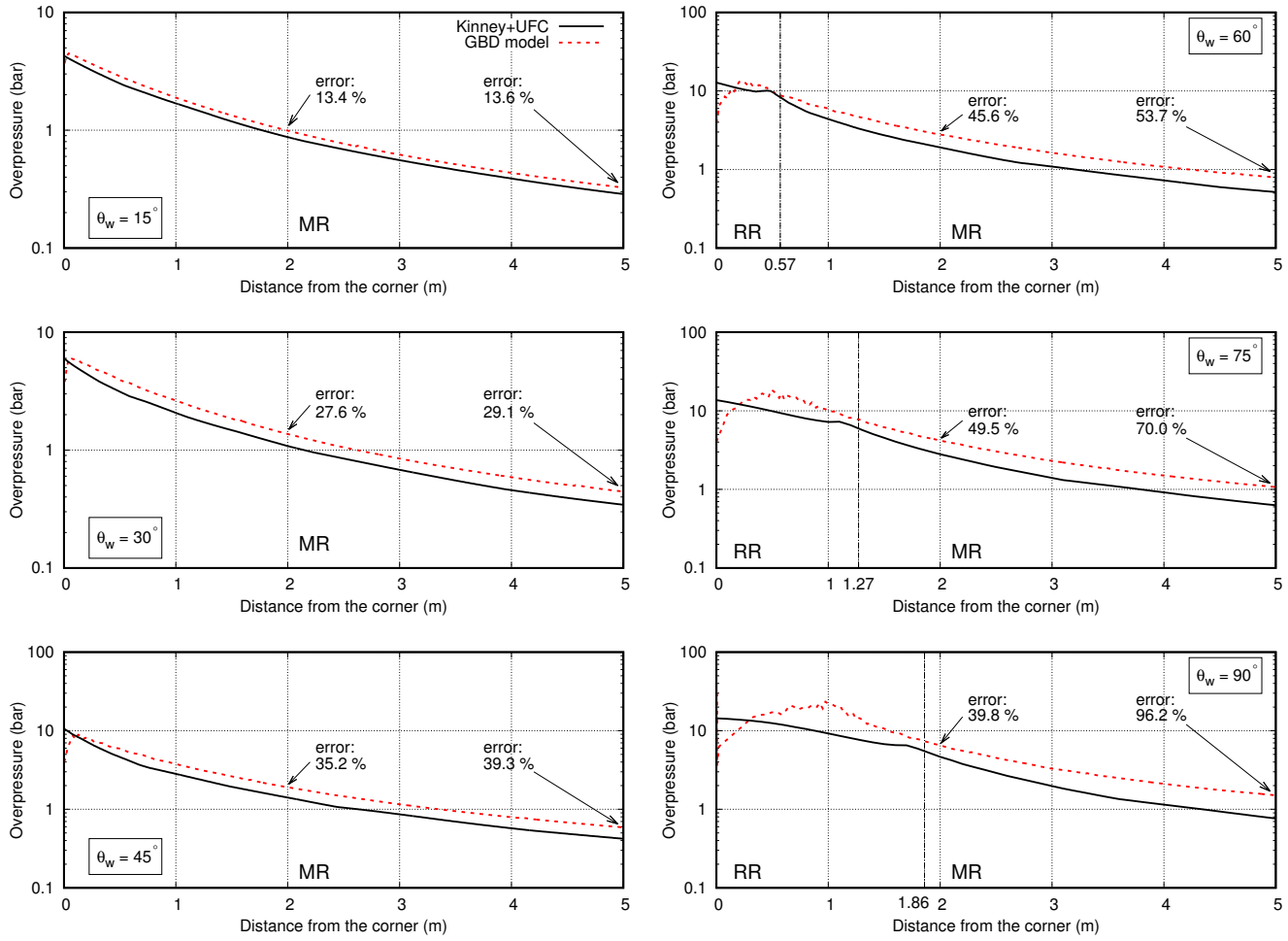

Fig. 15 Reflection of a spherical blast wave over a concave corner of deflection angle θ_w as sketched in figure 14. The structure is placed at $dist = 2$ m from TNT charge. Wall overpressure versus distance from the corner. Errors are calculated at 2 m and 5 m from the corner with relation (39).

Let us consider the reflection of a spherical blast wave over a concave corner of deflection angle $\theta_w > 0$ as sketched in figure 14. The blast wave is issue from the explosion of 1 kg of TNT at the ground. GBD model is closed with the empirical Kinney's law (1) for spherical charges. Consequently, the amplification of the blast wave over the ground is taking into account at twice the mass of TNT [1], that is 2 kg of TNT here. As discussed in section 4.1, GBD model systematically provides a Mach Reflection in this configuration (compressive flows).

The overpressure along the wall estimated with GBD model is compared with reference solutions for distances from the charge to the structure, $dist$, ranging from 1 m to 4 m and for deflection angles, θ_w, ranging from 15° to 90°. The length of the ramp is equals to 5 meters.

Results are extracted from simulations at 5 mm height. Parameters Δs, d_c and the height of extraction have little influence over results from a distance of 0.2 m from the corner. Reference solutions (wall peak overpressures) are obtained from Kinney's law (1) and the reflection table in figure 4.

Results for $dist = 2m$. Results for $dist = 2$ m are presented in figure 15. Errors at 2 m and 5 m from the corner are evaluated with relation (39). A good agreement between GBD model and reference solutions can be observed. For θ_w ranging from 15° to 45°, the interaction of the blast wave with the concave corner theoretically results in a Mach Reflection (MR) according to (3). One observes a relative error lower than 40% for theses cases. For $\theta_w \geq 60°$, the reflection is first regular (RR) and then leads to a Mach reflection. The discrepancy between GBD model and reference solutions increases with the later Mach stem arising. Indeed, for $\theta_w = 60°$, a MR arises around 0.57 m from the corner. The error at 5 m from the corner is evaluated at 53.7%. For $\theta_w = 90°$, the MR occurs farther from the corner, around 1.86 m, and the error is 96.2%. As underlined in the previous subsection, this discrepancy is a consequence of GBD to systematically make arise a Mach stem for compressive flows.

It should be noted that GBD model correctly describes the decay of peak overpressure with an increasing error along the wall. Moreover, one notes an overestimation of reflected overpressure in comparison with reference solutions. These observations are similar for $dist = 1$ m, $dist = 3$ m and $dist = 4$ m. All results are gathered in table 10 in appendix A.

Error analysis. The relative errors between GBD model and reference solutions at 2 m and 5 m from the corner are presented in figure 16. Although GBD model makes arise a Mach stem, errors do not increase with the later transition to MR. Indeed, for $\theta_w = 75°$ for example, the Mach stem arises around 0.57 m at $dist = 1$ m and around 1.27 m at $dist = 2$ from (3). Nevertheless, error at 5 m is higher at $dist = 1$ m than at $dist = 2m$: 132% versus 70%. It suggests that the gap between GBD model and reference solutions for compressive flows do not completely depends on the kind of reflection. Differences may come from the decoupling between local shock curvature changes and blast effects in the model. This point should be addressed in further investigations.

From error analysis at 2 m, three trends take shape depending on the kind of reflection:

- The interaction of the blast wave with the concave corner directly results in a Mach Reflection (MR).

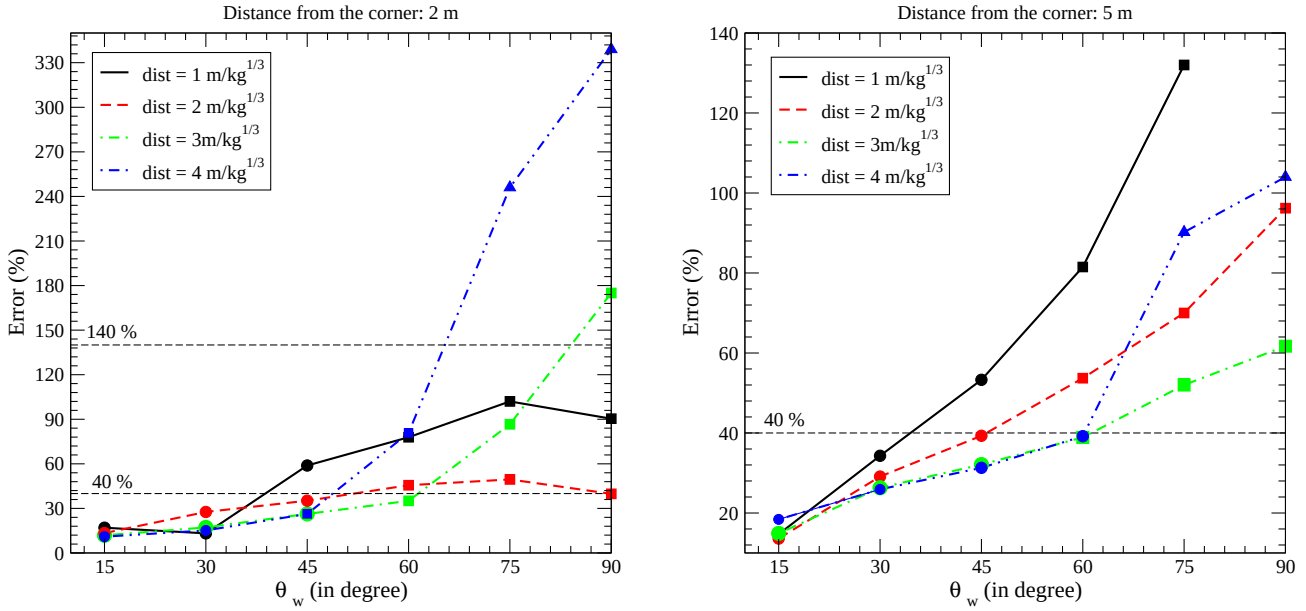

(a) (b)

Fig. 16 Reflection of a spherical blast wave over a concave corner as sketched in figure 14. Relative errors (39) for wall overpressure between GBD model and reference solutions (Kinney (1)+reflection coefficients, figure 4) at 2 m and 5 m from the corner. Circle points and triangular points correspond to MR and RR respectively, according to relation (3). Square points are configurations with a transition between RR and MR. Results are gathered in table 10 in appendix A.

For theses configurations, errors are mostly lower than 40%. It appears GBD model is in a good agreement with data for configurations where a Mach stem arises ;

- The reflection is first regular and then leads to a Mach Reflection (RR → MR). This change of reflection regime mostly leads to errors upper than 40% ;
- The reflection is only regular (RR) and errors are greater than 140%.

RR analysis. The trend of GBD model to produce a Mach stem for configurations where reflection is regular clearly leads to a drastic overestimation of blast wave damages (upper to 40% on wall overpressure). For example, for $dist = 4$ m and $\theta_w \geq 75°$ where the reflection is regular according to (3), the error at 2 m from the corner is larger than 200%. Figure 17 shows the wall overpressure in comparison to the overpressure extracted just above the shock-shock for RR configurations. This latter can be only evaluated when the Mach stem is numerically established: at 2 m from the corner for $\theta_w = 75°$ and at 2.7 m from the corner for $\theta_w = 90°$. Results at 5 m and 8 m from the corner are presented in table 2. The estimation of overpressure is significantly improved, with errors lower than 6% at 8

	Results at 5 m from the corner			Results at 8 m from the corner		
θ_w (°)	ΔP_w ref (bar)	ΔP_w GBD (bar)	ΔP_c GBD (bar)	ΔP_w ref (bar)	ΔP_w GBD (bar)	ΔP_c GBD (bar)
75	0.611	1.162 error: 90.2%	0.714 error: 16.9%	0.384	0.638 error: 60.1%	0.407 error: 5.99%
90	0.787	1.602 error: 104%	0.980 error: 24.5%	0.486	0.816 error: 67.9%	0.513 error: 5.56%

Table 2 Reflection of a spherical blast wave over a concave corner for $dist = 4$ m from the charge and with deflection angles of 75° and 90°. Comparison between wall overpressures, ΔP_w, and overpressures around 0.01 m above the shock-shock, ΔP_c.

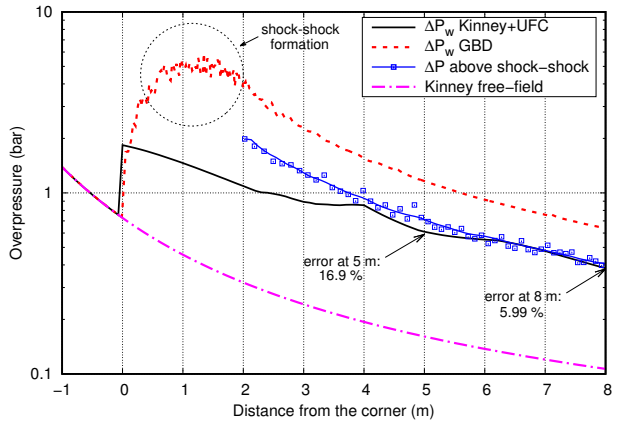

(a)

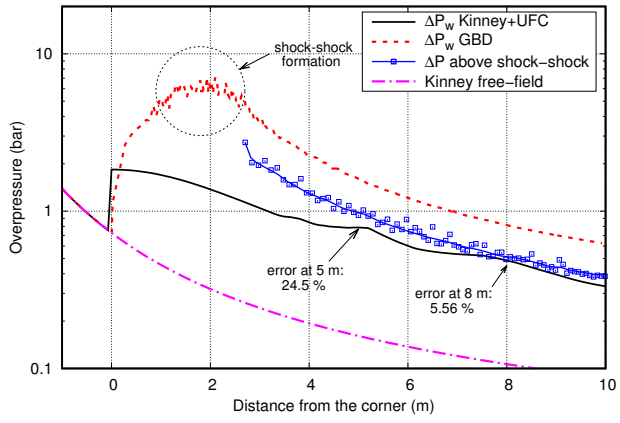

(b)

Fig. 17 Reflection of a spherical blast wave over a concave corner for $dist = 4$ m from the charge and with deflection angles $\theta_w = 75°$ (a) and $\theta_w = 90°$ (b). Comparison between wall overpressure and overpressure around 0.01 m above the shock-shock. Free field estimation (1) is drawn as an indication.

m from the corner. Accordingly, some additional mechanisms should be considered in GBD in order to remove Mach stem for RR configurations.

5.3 Diffraction of a spherical blast wave over a convex corner

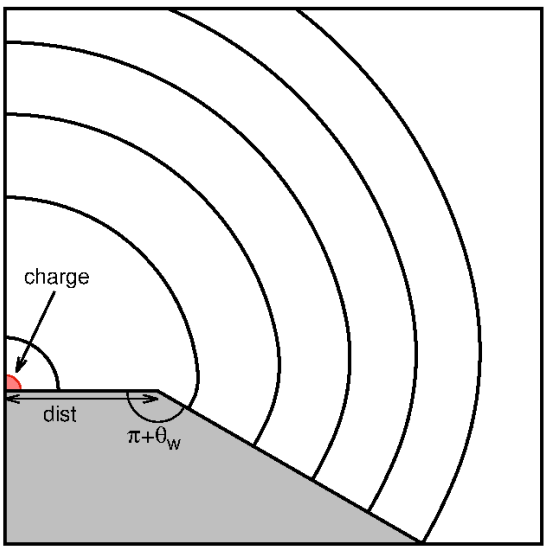

Fig. 18 Scheme a spherical blast wave diffraction over a convex corner.

Results are extracted from simulations at 5 mm height. The parameter d_c is not necessary in this con-

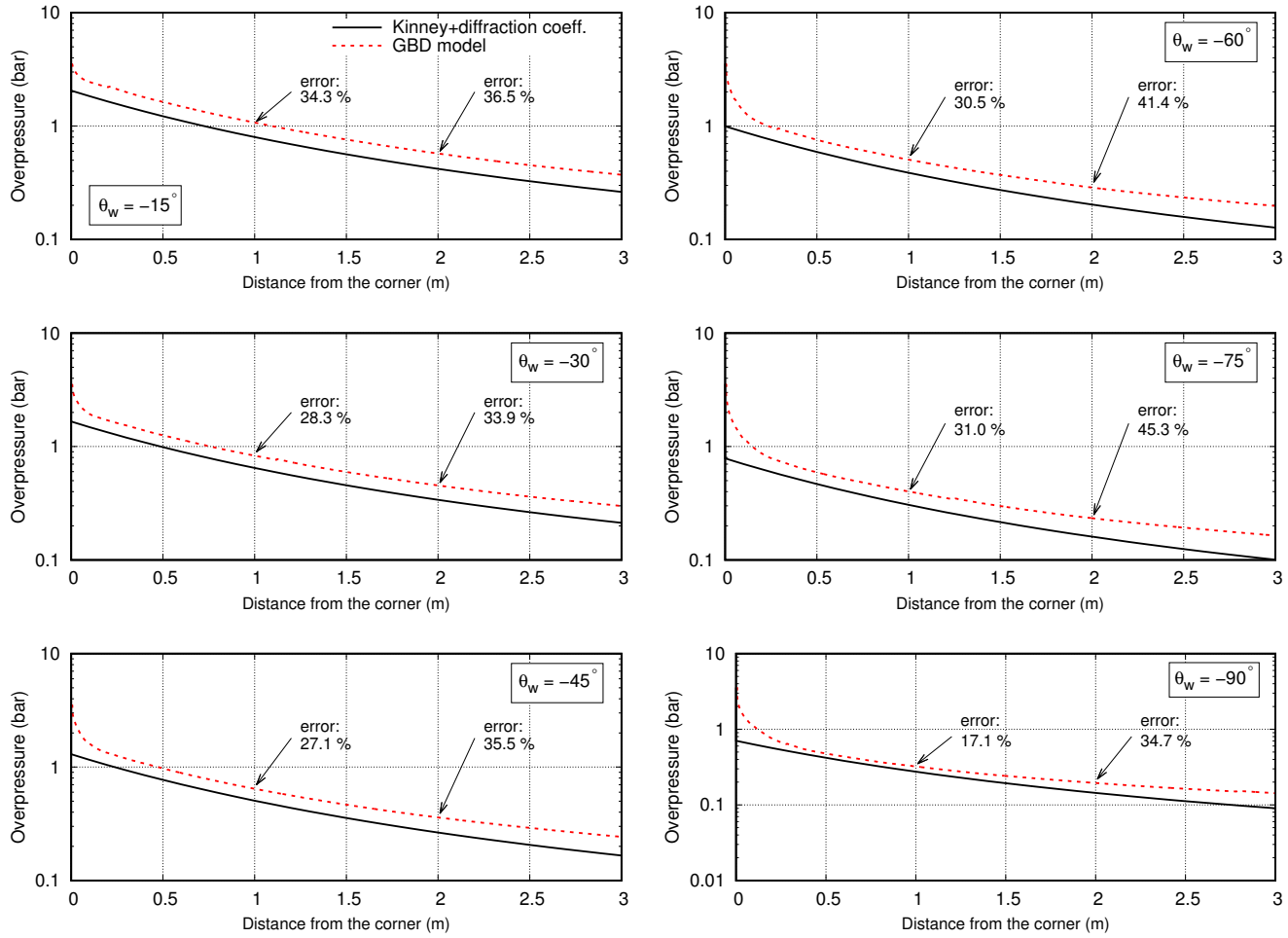

Fig. 19 Diffraction of a spherical blast wave over a convex corner of deflection angle θ_w as sketched in figure 18. The structure is placed at $dist = 2$ m from TNT charge. Wall overpressure versus distance from the corner. Errors are calculated at 1 m and 2 m from the corner with relation (39).

figuration as no shock-shocks appear (expansive flows). Δs and the height of extraction have little influence over results from a distance of 0.2 m from the corner. Reference solutions (wall peak overpressures) are obtained from Kinney's law (1) and diffraction coefficients table in figure 5(b).

Let us consider the diffraction of a spherical blast wave over a convex corner of deflection angle $\theta_w < 0$ as sketched in figure 18. The blast wave is issue from the explosion of 1 kg of TNT at the ground. GBD model is closed with the empirical Kinney's law (1) for spherical charges. Consequently, the amplification of the blast wave over the ground is taking into account at twice the mass of TNT [1], that is 2 kg of TNT here.

The overpressure along the wall estimated with GBD model is compared with reference solutions for distances

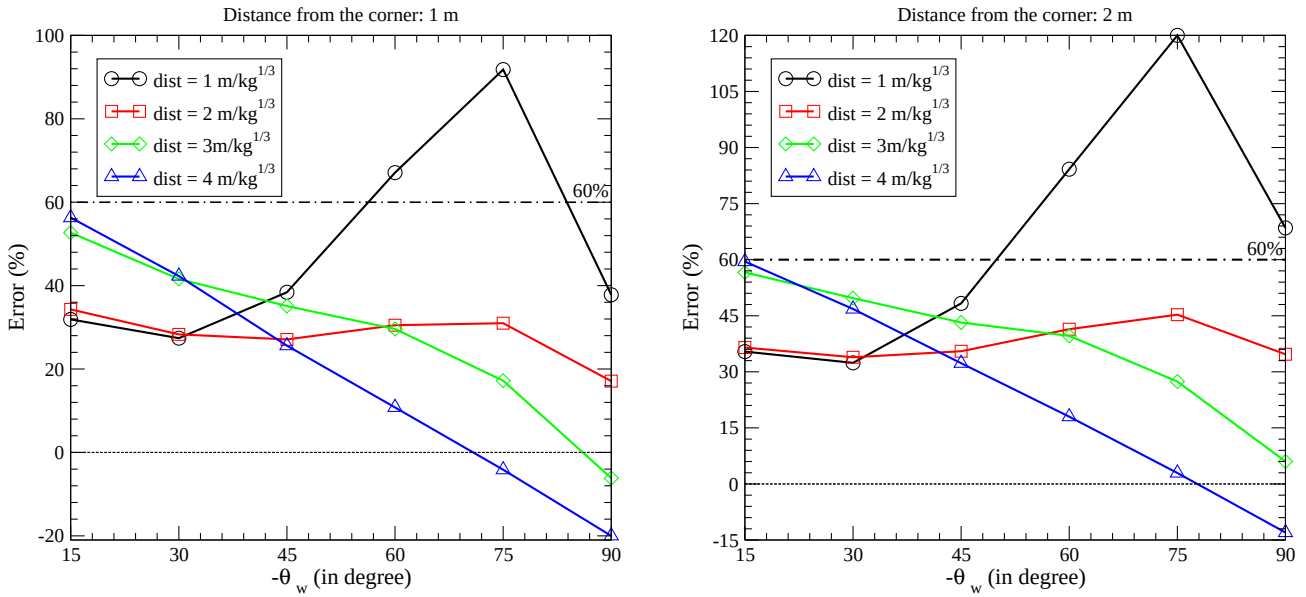

(a) (b)

Fig. 20 Diffraction of a spherical blast wave over a convex corner as sketched in figure 18. Relative errors (39) for wall overpressure between GBD model and reference solutions (Kinney (1)+diffraction coefficients, figure 5(b)) at 1 m and 2 m from the corner. Results are gathered in table 11 in appendix A.

from the charge to the structure, *dist*, ranging from 1 m to 4 m and for deflection angles, θ_w, ranging from $-15°$ to $-90°$. The length of the ramp is equals to 3 meters.

Results for dist = 2m. Results for *dist* = 2 m are presented in figure 19. Errors at 1 m and 2 m from the corner are calculated with relation (39). A good agreement between GBD model and reference solutions is observed with an overestimation of the wall overpressure up to 45%. The decay of peak overpressure along the wall is correctly describes by GBD model, but with an increasing error along the wall. This observation is similar for *dist* = 1 m, *dist* = 3 m and *dist* = 4 m. All results are gathered in table 11 in appendix A.

Error analysis. The relative error between GBD and reference solutions at 1 m and 2 m from the corner are presented in figure 20. For $\theta_w \leq 45°$, errors increase with the distance from the charge, *dist*. The trend is reversed for $\theta_w \geq 60°$ with an underestimation of wall overpressure in comparison with data for $\theta_w \geq 75°$ and *dist* = 4 m. For *dist* = 1 m, GBD model drastically overestimates the wall overpressure up to twice that estimated by the reference solutions. From *dist* = 2 m, errors are limited by 60%.

$dist$ (m)	1	2	3	4
M_0	3.86	2.00	1.47	1.27

Table 3 Incident Mach number at the corner according to (1) and (6) for $W = 1.0$ kg of TNT at the ground, *i.e.* $W = 2.0$ kg.

The gap between GBD results and reference values may come from the discrepancy between GSDT and experiments as observed in figure 9. Indeed, for $\theta_w = -75°$ for example, the gap between GSDT model and experiments is more important for $M_0 = 4$ than for $M_0 = 2$. Incident Mach number, M_0, decreases when the charge is farther from the structure as seen in table 3. For $\theta_w = -75°$, the gap between GBD model and reference solutions are larger for $dist = 1$ m where $M_0 = 3.86$ than for $dist = 2$ m where $M_0 = 2$, as underlined for GSDT.

5.4 Interaction of a spherical blast wave with a mound

As a last example, let us consider the interaction of an hemispherical blast wave generated by a gaseous charge (stoichiometric propane-oxygen mixture) with a protective barrier, also called a mound. This study comes from [3, 38] in which small-scale experiments are carried out (scale 1/15). Figure 21 shows the schematic representation of the experimental bench. The r_0 radius charge is placed at the distance d from the mound and it releases an energy E. The mound is characterized by its height, h, the top thickness, e, the front side inclination angle, α_1, and the back side inclination angle, α_2. In [38], captors are located on each face of the barrier (numbered from Gi1 to Gi5 or Gi6) and behind the mound (GH1 to GH7) which record the peak overpressure. This experimental results are compared with 2D-axisymmetrical Eulerian simulations. These latter ones required 256 processors on the TERA100 supercomputer during 12 hours [3].

We propose here to compare the history of the wall peak overpressure between GBD model, the Eulerian results and the experimental data. The features for each case treated in this section are gathered in table 4. Two charges are considered, referred as C3 and C6 with a radius of 3 cm and 6 cm respectively. Two kinds of mound are treated so-called 1A and 1B as shown in figure 21. Both mounds differ in the top thickness, e, and the back side inclination angle, α_2. The different faces of the mound and the ground behind it are numbered from 1 to 4 as shown in figure 23(a). The detonation of the charge generates a blast wave in the air which interacts with the mound. The shock interaction with the obstacle results in four successive reflection or diffraction : reflection on the faces 1 and 4 and diffraction on the faces 2 and 3.

GBD model is closed with the stoichiometric propane-oxygen gas law (2). For Lagrangian simulations, we sug-

Case	r_0 (m)	E (MJ)	d (m)	α_1 (°)	α_2 (°)	e (m)	h (m)
1AC3d8,5	0.03	1.72×10^{-3}	0.085	45	45	0.03	0.19
1AC6d7	0.06	13.75×10^{-3}	0.070	45	45	0.03	0.19
1BC6d7	0.06	13.75×10^{-3}	0.070	45	90	0.19	0.19
1BC6d14	0.06	13.75×10^{-3}	0.140	45	90	0.19	0.19

Table 4 Features for cases from [38] as seen in figure 21. Cases are called as the original ones for consistency.

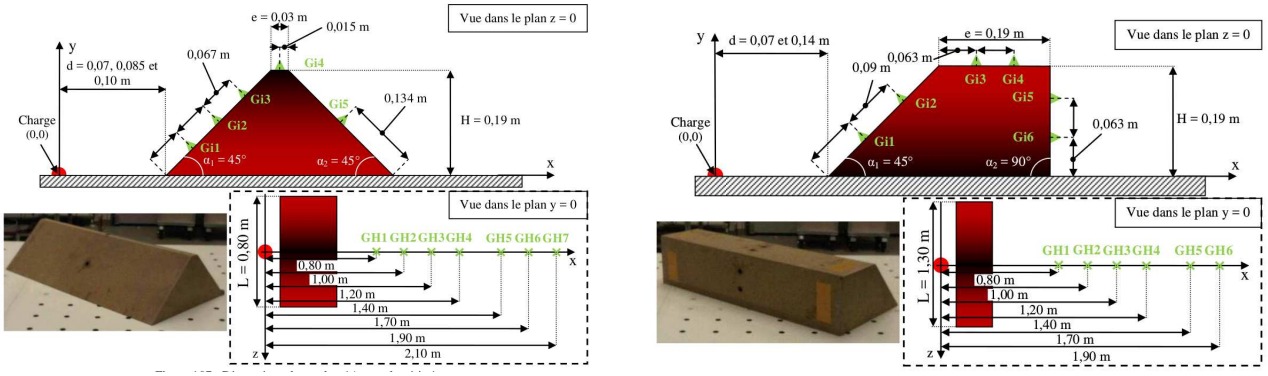

(a) (b)

Fig. 21 Schematic representation of test bench of small-scale experiments from [38] for mound 1A (a) and mound 1B (b).

Case/Δs (m)	10.0×10^{-4}	5.0×10^{-4}	2.5×10^{-4}
1AC3d8,5 $t_f = 2.031$ ms	/	1 min 10 s	4 min 45 s
1AC6d7 $t_f = 6.100$ ms	2 min 25	9 min 40 s	/
1B6d7 $t_f = 5.420$ ms	1 min 50 s	8 min 00 s	/
1B6d14 $t_f = 5.420$ ms	1 min 40 s	7 min 45 s	/

Table 5 Computational time to solve GBD model with the Lagrangian algorithm. Simulation made on *Intel(R) Core(TM) i5-8300H CPU @ 2.30GHz*. t_f is the simulated time.

gest to discretize the initial hemispherical shock wave with one point per degree, that is a space step, Δs, equals to 5.0×10^{-4} m for charge C3 and 10.0×10^{-4} m for charge C6. This point will be discussed hereafter. The Lagrangian simulations have been performed with $d_c = 0.02$ and results are extracted from simulations at $2\Delta s$ height. We recall that shock wave reflection with GBD results in a TP arising.

Computational time for each case are given in table 5 for several space steps, Δs. One points out that only a few minutes are necessary to solve the problem, while Eulerian simulations requires 12 hours.

Case 1AC3d8,5. Results on the faces 1 to 3 are drawn in figure 22. GBD model slightly overestimates wall overpressure in comparison with experimental data and Eulerian simulations. The table 6 gathered peak over-

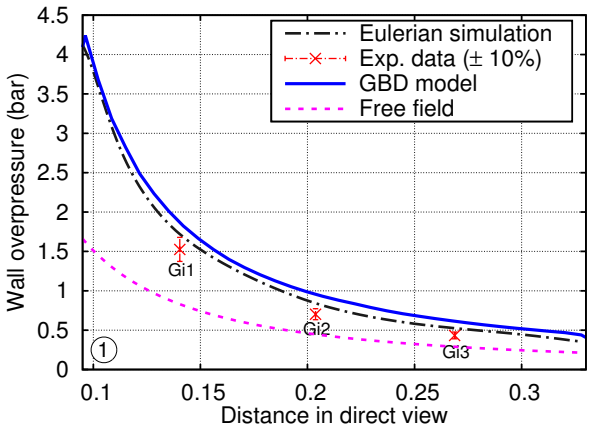

(a)

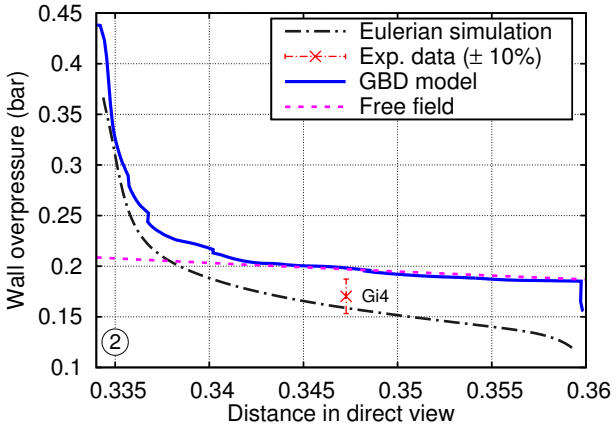

(b)

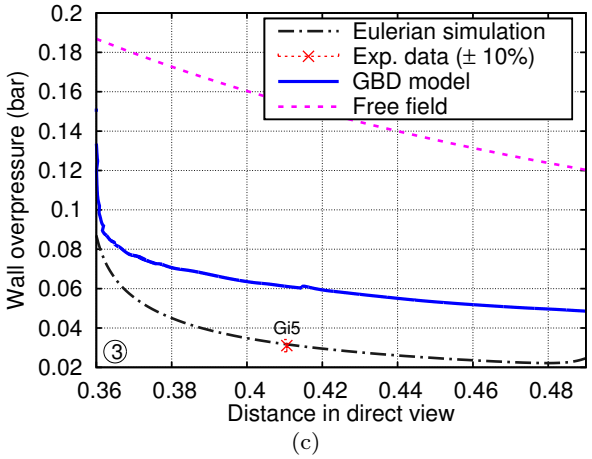

(c)

Fig. 22 Case 1AC3d8,5. Wall peak overpressure on the front side (a), the top side (b) and the back side (c) of the barrier. Eulerian and experimental data are taken from [38]. The free field estimation comes from (2). The Lagrangian simulation has been performed with $\Delta s = 2.5 \times 10^{-4}$ m.

pressure at the captors. In light of the results, $\Delta s = 5.0 \times 10^{-4}$ m is enough to achieve nearly-converged results. Errors for GBD increase as the blast wave travels on the face 1, from 22.4% to 42.5%. The error is low after the diffraction over the top side, with only 18.8% at the captor Gi4. At the captor Gi5, after the second diffraction, GBD model overestimates the wall overpressure up to twice that recorded by the captor. Nevertheless, one can notice that results are good in comparison with a free field estimation (2), as well as in view of the computational time: around 1 minute with GBD model versus 12 hours with an Eulerian simulation.

Case 1AC6d7. The successive shock positions calculated with the Lagrangian scheme are drawn in figure 23(a). Two shock-shock trajectories (Triple Points) can be observed: the first one when the shock reflects over the front side of the barrier (face 1) and the second one when it interacts with the ground (face 4). Results for wall peak overpressure from the faces 1 to 4 are drawn in figure 23(b)-(e). For the faces 1 to 3, GBD model slightly overestimates wall overpressure in comparison with experimental data and Eulerian simulations. A large overestimation occurs behind the barrier (face 4). This discrepancy is a consequence of GBD to systematically produce a Mach stem for compressive

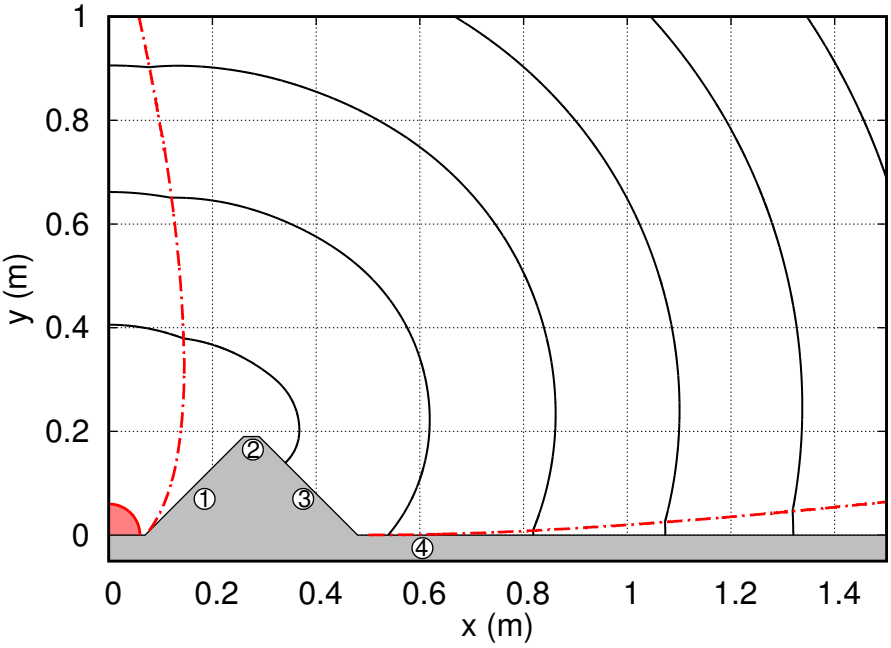

(a)

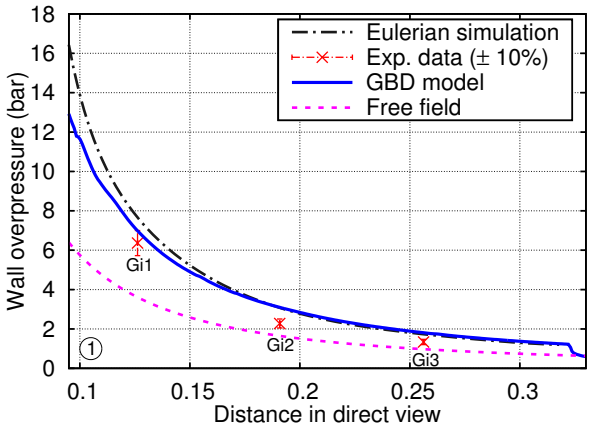

(b)

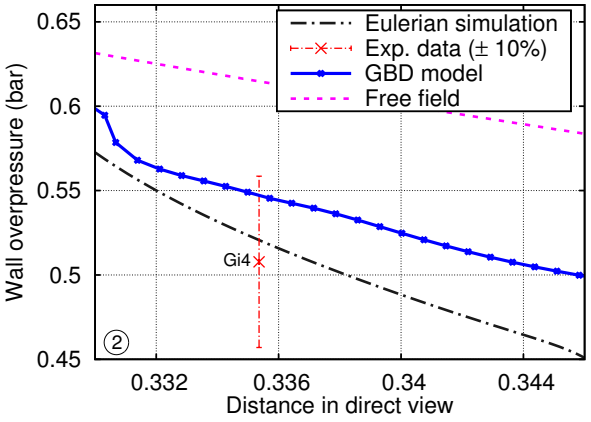

(c)

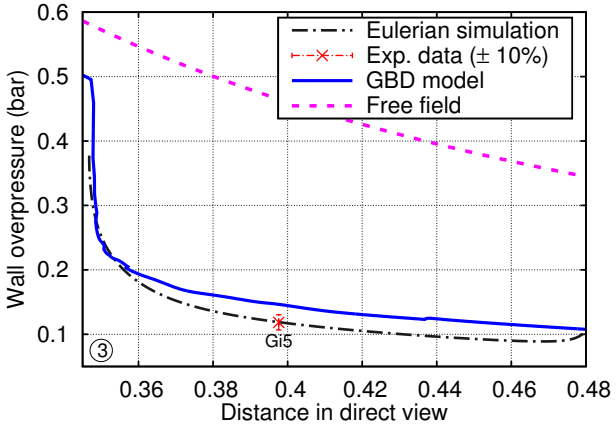

(d)

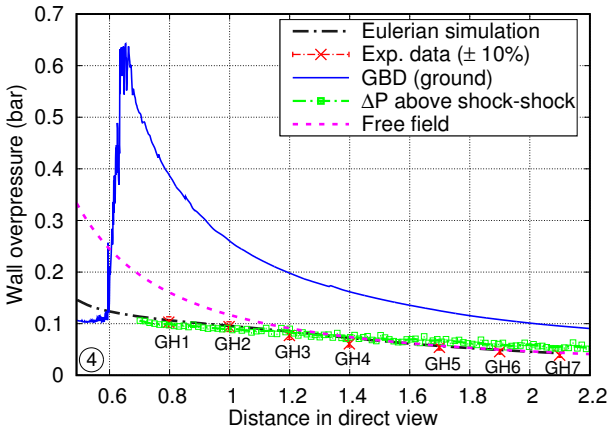

(e)

Fig. 23 Case 1AC6d7. Successive shock front positions (a) (red dashed lines correspond to TP paths) and wall peak overpressure on each face of the barrier (b)-(e). Eulerian and experimental data are taken from [38]. The free field estimation comes from (2). The Lagrangian simulation has been performed with $\Delta s = 5.0 \times 10^{-4}$ m.

			ΔP_{w} GBD (bar)		Error for
Face	Captors	ΔP_{w} exp. (bar)	$\Delta s = 5.0 \times 10^{-4}$ m	$\Delta s = 2.5 \times 10^{-4}$ m	$\Delta s = 5.0 \times 10^{-4}$
1	Gi1	1.520	1.860	1.870	22.4%
	Gi2	0.703	0.952	0.957	35.4%
	Gi3	0.433	0.617	0.614	42.5%
2	Gi4	0.170	0.202	0.193	18.8%
3	Gi5	0.031	0.061	0.061	96.8%

Table 6 Case 1AC3d8,5. Peak overpressure at the captors (seen figure 21(a) for captors positions). Errors are calculated with relation (39).

			$\Delta P_{\mathrm{w}}/\Delta P_{\mathrm{c}}$ GBD (bar)		Error for
Face	Captors	ΔP_{w} exp. (bar)	$\Delta s = 10.0 \times 10^{-4}$ m	$\Delta s = 5.0 \times 10^{-4}$ m	$\Delta s = 10.0 \times 10^{-4}$
1	Gi1	6.360	6.85	6.99	7.70%
	Gi2	2.280	3.07	3.10	34.6%
	Gi3	1.340	1.81	1.81	35.1%
2	Gi4	0.508	0.604	0.549	18.9%
3	Gi5	0.120	0.142	0.145	18.3%
4	GH1	0.102	0.096	/	−5.9%
	GH2	0.094	0.086	/	−8.5%
	GH3	0.077	0.079	/	−2.5%
	GH4	0.061	0.070	/	14.8%
	GH5	0.054	0.061	/	13.0%
	GH6	0.045	0.056	/	24.4%
	GH7	0.039	0.052	/	33.3%

Table 7 Case 1AC6d7. Peak overpressure at the captors (seen figure 21(a) for captors positions). Results at the face 4 correspond to overpressure around $2\Delta s$ above the shock-shock and they are similar for $\Delta s = 5.0 \times 10^{-4}$ m. Errors are calculated with relation (39).

flows, while the reflection is regular in this configuration. However, the overpressure extracted around $2\Delta s$ above the shock-shock is in excellent agreement with data.

The table 7 gathered peak overpressure at the captors. In light of the results, $\Delta s = 10.0 \times 10^{-4}$ m is enough to achieve nearly-converged results. Errors for GBD increase as the blast wave travels on the face 1, from 7.70% to 35.1%. The error is low after the diffrac-

Case	Face	Captors	ΔP_{w} exp. (bar)	ΔP_{w} GBD (bar)	Error
1BC6d7	2	Gi3	0.370	0.430	16.2%
		Gi4	0.281	0.342	21.7%
	3	Gi5	0.053	0.065	22.6%
		Gi6	0.040	0.055	37.5%
1BC6d14	2	Gi3	0.321	0.388	20.5%
		Gi4	0.242	0.316	30.6%
	3	Gi5	0.048	0.058	20.9%
		Gi6	0.038	0.050	31.6%

Table 8 Cases 1BC6d7 and 1BC6d14. Peak overpressure at the captors (seen figure 21(b) for captors positions). The Lagrangian simulation has been performed with $\Delta s = 10.0 \times 10^{-4}$ m. Errors are calculated with relation (39).

tion over the top side and the back side: 18.9% at the captor Gi4 and 18.3% at the captor Gi4. Behind the barrier, the overpressure extracted above the shock-shock is in good agreement with data, with errors from -8.5% to 33.3%. Accordingly, some additional mechanisms should be considered in GBD in order to account for the regular reflection, especially for weak shocks. In the light of the results and the computational time (around 2 minutes with GBD model versus 12 hours with an Eulerian simulation), wall overpressures are correctly predicted by GBD model.

Cases 1BC6d7 and 1BC6d14. Configuration of the mound 1B is shown in figure 21(b). This configuration implies a more important blast wave mitigation on the faces 2 and 3 than the precedent one (mound 1A). Results for wall peak overpressure at the faces 2 and 3 are presented in table 8. $\Delta s = 10.0 \times 10^{-4}$ m is enough to achieve nearly-converged results. Once again, GBD model overestimates the wall overpressure in comparison with experimental data. For both cases, errors for GBD increase as the blast wave travels on the face 2 and on the face 3. Errors do not exceed 38%. In the light of the results and the computational time (less than 2 minutes with GBD model versus 12 hours with an Eulerian simulation), GBD model is in excellent with experimental data.

6 Conclusion and perspectives

In this paper, a simplified model aiming at simulating blast waves propagation at low computational cost has been presented. This new approach is based on a simple extension of GSDT model (Geometrical Shock Dynamics with extended to transverse flow) to blast waves through an *ad-hoc* closure. It consists in mod-

elling the post-shock flow with an empirical law for spherical charges, instead of neglecting it as in the original model. The new model, named Geometrical Blast Dynamics (GBD), takes into account simply any type of source and interactions with obstacles.

GBD model has been evaluated on a wide range of problems from simple configurations, such that reflection or diffraction over a corner, to more complex geometries such that interaction with mounds. The analysis of the results in comparison with experimental data, semi-empirical models from the literature and Eulerian simulations shows the ability of GBD to estimate correctly blast waves propagation interacting with obstacles. Moreover, the computational time is drastically reduced: a few minutes with one processor, while Eulerian simulations requires hours on several processors. GBD model overestimates overpressure, which is better worth in a pyrotechnic hazard context. This trend is reinforced in compressive flows as GBD makes arise a Mach stem even for regular reflection. This default is corrected if overpressure is extracted above the Mach stem. This means that some additional mechanisms should be implemented in GBD in order to account for the regular reflection, especially for weak shocks.

In the future, GBD model should be extended to regular reflection and experienced on more complex configurations. Moreover, GBD model only gives the peak overpressure. A simple modelling of the positive phase may be studied. At last, a three-dimensional extension could be envisaged. These issues could be addressed in further investigations.

Acknowledgements Part of this work has been possible thanks to the LETMA collaboration: a contractual research laboratory between CEA, CNRS, École Centrale Lyon, C-Innov and Université Pierre et Marie Curie.

References

1. G.F. Kinney and K.J. Graham. *Explosive shocks in air*. Springer Science & Business Media, 2013.
2. Air Force Civil Engineer Support Agency US Army Corps of Eng. Naval Facil. Eng. Command. Unified Facilities Criteria (UFC) 3-340-02: Structures to resist the effect of accidental explosions. 2008.
3. S. Éveillard, N. Lardjane, J.Y. Vinçont, and I. Sochet. Towards a fast-running method for blast-wave mitigation by a prismatic blast wall. *Comptes Rendus Mécanique*, 341(8):625–635, 2013.
4. M. Silvestrini, B. Genova, and F.J. Leon Trujillo. Energy concentration factor. a simple concept for the prediction of blast propagation in partially confined geometries. *Journal of Loss Prevention in the Process Industries*, 22(4):449–454, 2009.
5. C.E. Needham. Blast wave propagation. In *Blast Waves*, pages 87–99. Springer, 2010.

6. J. Boutillier, L. Ehrhardt, S. De Mezzo, C. Deck, P. Magnan, P. Naz, and R. Willinger. Evaluation of the existing triple point path models with new experimental data: proposal of an original empirical formulation. *Shock Waves*, pages 1–10, 2017.
7. P. Miller. *Towards the modelling of blast loads on structures*. University of Toronto, 2004.
8. E. Lapébie, R. Soulié, and L. Youinou. Flash : Fast lethality assessment for structures and humans. In *Proceedings of the Military Aspects of Blast and Shock*, 2016.
9. I. Flood, B.T. Bewick, and R.J. Dinan. A new method for very fast simulation of blast wave propagation in complex built environments. Technical report, DTIC Document, 2010.
10. G.B. Whitham. A new approach to problems of shock dynamics. Part I: Two-dimensional problems. *Journal of Fluid Mechanics*, 2(2):145–171, 1957.
11. G.B. Whitham. A new approach to problems of shock dynamics. Part II: Three-dimensional problems. *Journal of Fluid Mechanics*, 5(3):369–386, 1959.
12. G.B. Whitham. In *Linear and Nonlinear Waves*, chapter 8: Shock Dynamics. John Wiley & Sons, Inc., 3rd edition, 1999.
13. J.P. Best. A generalisation of the theory of Geometrical Shock Dynamics. *Shock Waves*, 1(4):251–273, 1991.
14. D.W. Schwendeman and G.B. Whitham. On converging shock waves. In *Proceedings of the Royal Society of London A: Mathematical, Physical and Engineering Sciences*, volume 413, pages 297–311, 1987.
15. D.W. Schwendeman. On converging shock waves of spherical and polyhedral form. *Journal of Fluid Mechanics*, 454:365–386, 2002.
16. C.J. Catherasoo and B. Sturtevant. Shock dynamics in non-uniform media. *Journal of Fluid Mechanics*, 127:539–561, 1983.
17. C. Besset and E. Blanc. Propagation of vertical shock waves in the atmosphere. *The Journal of the Acoustical Society of America*, 95(4):1830–1839, 1994.
18. B.W. Skews. The shape of a diffracting shock wave. *Journal of Fluid Mechanics*, 29(02):297–304, 1967.
19. T.V. Bazhenova, L.G. Gvozdeva, and Y.V. Zhilin. Change in the shape of the diffracting shock wave at a convex corner. *Acta Astronautica*, 6(3):401–412, 1979.
20. V.D. Sharma and C. Radha. On one-dimensional planar and nonplanar shock waves in a relaxing gas. *Physics of Fluids*, 6(6):2177–2190, 1994.

21. V.D. Sharma and C. Radha. Three dimensional shock wave propagation in an ideal gas. *International Journal of Non-Linear Mechanics*, 30(3):305–322, 1995.

22. M. Pandey and V.D. Sharma. Kinematics of a shock wave of arbitrary strength in a non-ideal gas. *Quarterly of Applied Mathematics*, 67(3):401–418, 2009.

23. J. Ridoux, N. Lardjane, L. Monasse, and F. Coulouvrat. Comparison of Geometrical Shock Dynamics and Kinematic models for shock wave propagation. *Shock Waves*, 27(5):1–16, 2017.

24. K. Oshima, K. Sugaya, M. Yamamoto, and T. Totoki. Diffraction of a plane shock wave around a corner. *ISAS report*, 30(2):51–82, 1965.

25. K. Oshima. Propagation of spacially non-uniform shock waves. *ISAS report*, 30(6):195, 1965.

26. J. Ridoux, N. Lardjane, L. Monasse, and F. Coulouvrat. Beyond the limitation of geometrical shock dynamics for diffraction over wedges. *Shock Waves*, pages 1–23, 2019.

27. J.T. Peace and F.K. Lu. On the propagation of decaying planar shock and blast waves through non-uniform channels. *Shock Waves*, pages 1–15, 2018.

28. Michael M. Jr. Swisdak. Simplified kingery airblast calculations. In *Minutes of the 26th DOD explosives safety seminar*. 1994. Accessed 16 January 2017.

29. G. Ben-Dor. In *Handbook of Shock Waves*, volume 2, chapter 8.1: Oblique Shock Wave Reflections, pages 68–179. Academic Press, 2000.

30. M. McKinzie, T.B. Cochran, R.S. Norris, and W.M. Arkin. *The US nuclear war plan: A time for change*. Natural Resources Defense Council Washington, DC, 2001.

31. R. Courant and K.O. Friedrichs. *Supersonic flow and shock waves*, volume 21. Springer Science & Business Media, 1999.

32. W.D. Henshaw, N.F. Smyth, and D.W. Schwendeman. Numerical shock propagation using geometrical shock dynamics. *Journal of Fluid Mechanics*, 171:519–545, 1986.

33. G. Taylor. The formation of a blast wave by a very intense explosion. i. theorical discussion. *Proceedings of the Royal Society of London. Series A, Mathematical and Physical Sciences*, pages 159–174, 1950.

34. H.T. Huynh. Accurate monotone cubic interpolation. *SIAM Journal on Numerical Analysis*, 30(1):57–100, 1993.

35. S. Gottlieb and C.W. Shu. Total variation diminishing runge-kutta schemes. *Mathematics of computation of the American Mathematical Society*, 67(221):73–85, 1998.

36. H. Jourdren. HERA: a hydrodynamic AMR platform for multi-physics simulations. In *Adaptive Mesh Refinement-Theory and Applications*, pages 283–294. Springer, 2005.

37. W.E. Lorensen and H.E. Cline. Marching cubes: A high resolution 3d surface construction algorithm. In *ACM siggraph computer graphics*, volume 21, pages 163–169. ACM, 1987.

38. S. Éveillard. *Propagation d'une onde de choc en présence d'une barrière de protection*. PhD thesis, Université d'Orléans, 2013.

A Results for blast wave reflection over a concave corner and blast wave diffraction over a convex corner

Numerical results for reflection of a spherical blast wave over a concave corner, as explained in section 5.2, are gathered in tables 10. 2D-axisymmetrical Lagrangian simulations have been performed with $\Delta s = 0.005$ m and $d_c = 0.05$ m. For $dist = 1$ m and $\theta_w = 90°$, the shock-shock reflects over the axis of symmetry and perturbs results at 5 meters from the corner.

Numerical results for diffraction of a spherical blast wave over a convex corner, as explained in section 5.3, are gathered in tables 11. 2D-axisymmetrical Lagrangian simulations have been performed with $\Delta s = 0.005$ m and $d_c = 0.05$ m.

Incident overpressures and incident Mach numbers are given in table 9 as an indication.

$dist$ (m)	1	2	3	4
ΔP_i (bar)	16.43	3.562	1.387	0.727
M_i	3.86	2.00	1.47	1.27

Table 9 Interaction of a spherical shock wave over a convex or a concave corner. Incident overpressures (1), ΔP_i, and incident Mach numbers (6), M_i, at the corner for $W = 1.0$ kg of TNT at the ground, *i.e.* $W = 2.0$ kg.

		Transition RR→MR			Results at 2 m from the corner			Results at 5 m from the corner			
dist (m)	θ_w (°)	R_0 (m)	ΔP_i (bar)	β_i (°)	ΔP_w GBD (bar)	ΔP_w ref (bar)	Error (%)	ΔP_w GBD (bar)	ΔP_w ref (bar)	Error (%)	Regime of reflection
1	15	0.00	16.43	75.0	1.813	1.549	17.0	0.406	0.354	14.7	MR
	30	0.00	16.43	60.0	2.000	1.767	13.2	0.523	0.396	34.3	MR
	45	0.00	16.43	45.0	3.180	2.004	58.9	0.664	0.433	53.3	MR
	60	0.24	12.47	40.7	4.330	2.434	77.9	0.864	0.476	81.5	RR then MR
	75	0.57	9.830	40.8	6.140	3.043	102.0	1.256	0.541	132.0	RR then MR
	90	0.86	9.100	40.8	11.49	6.036	90.4	AXI. EFFECTS			RR then MR
2	15	0.00	3.562	75.0	0.992	0.875	13.4	0.326	0.287	13.6	MR
	30	0.00	3.562	60.0	1.370	1.080	27.6	0.444	0.344	29.1	MR
	45	0.00	3.562	45.0	1.907	1.410	35.2	0.588	0.422	39.3	MR
	60	0.57	2.476	42.2	2.784	1.912	45.6	0.793	0.516	53.7	RR then MR
	75	1.27	1.879	42.8	4.180	2.796	49.5	1.071	0.630	70.0	RR then MR
	90	1.86	1.719	43.0	6.503	4.650	39.8	1.501	0.765	96.2	RR then MR
3	15	0.00	1.387	75.0	0.657	0.587	11.9	0.278	0.242	14.9	MR
	30	0.00	1.387	60.0	0.952	0.812	17.2	0.399	0.316	26.3	MR
	45	0.00	1.387	45.0	1.408	1.115	26.3	0.552	0.418	32.1	MR
	60	1.14	0.861	45.5	2.188	1.620	35.1	0.768	0.553	38.9	RR then MR
	75	2.35	0.633	47.2	3.796	2.034	86.6	1.090	0.717	52.0	RR then MR
	90	3.32	0.572	47.9	6.614	2.403	175.0	1.467	0.907	61.7	RR then MR
4	15	0.00	0.727	75.0	0.493	0.444	11.0	0.251	0.212	18.4	MR
	30	0.00	0.727	60.0	0.750	0.651	15.2	0.370	0.294	25.9	MR
	45	0.18	0.679	46.8	1.200	0.950	26.3	0.545	0.415	31.3	RR then MR
	60	2.50	0.356	52.3	2.000	1.106	80.8	0.796	0.572	39.2	RR then MR
	75	-	-	-	3.790	1.094	246.0	1.162	0.611	90.2	RR
	90	-	-	-	6.032	1.375	339.0	1.602	0.787	104.0	RR

Table 10 Spherical blast wave reflection over a concave corner as sketched in figure 14. Wall overpressure values, ΔP_w, are extracted from simulations at 5 mm height. Reference solutions are calculated from Kinney's law (1) and empirical reflection coefficients from UFC [2] (see figure 4). R_0: distance from the corner where a Mach stem arises, ΔP_i: incident overpressure (calculated with (1)), β_i: angle of incidence. The regime of reflection (RR: Regular Reflection, MR: Mach Reflection) are evaluated with (3). Errors are calculated with (39).

		Results at 1 m from the corner			Results at 2 m from the corner		
dist (m)	θ_w (°)	ΔP_w GBD (bar)	ΔP_w ref (bar)	Error (%)	ΔP_w GBD (bar)	ΔP_w ref (bar)	Error (%)
1	-15	2.690	2.039	31.9	1.070	0.790	35.4
	-30	2.049	1.608	27.4	0.829	0.626	32.4
	-45	1.569	1.134	38.4	0.654	0.441	48.3
	-60	1.218	0.729	67.1	0.523	0.284	84.2
	-75	0.963	0.502	91.8	0.431	0.196	120.0
	-90	0.787	0.571	37.8	0.374	0.222	68.5
2	-15	1.074	0.800	34.3	0.572	0.419	36.5
	-30	0.830	0.647	28.3	0.454	0.339	33.9
	-45	0.643	0.506	27.1	0.359	0.265	35.5
	-60	0.505	0.387	30.5	0.287	0.203	41.4
	-75	0.401	0.306	31.0	0.234	0.161	45.3
	-90	0.322	0.275	17.1	0.194	0.144	34.7
3	-15	0.571	0.374	52.7	0.368	0.235	56.6
	-30	0.446	0.315	41.6	0.292	0.195	49.7
	-45	0.350	0.259	35.1	0.232	0.162	43.2
	-60	0.276	0.213	29.6	0.187	0.134	39.6
	-75	0.218	0.186	17.2	0.149	0.117	27.4
	-90	0.183	0.195	-6.15	0.123	0.116	6.03
4	-15	0.361	0.233	56.3	0.260	0.163	59.5
	-30	0.286	0.201	42.3	0.207	0.141	46.8
	-45	0.221	0.176	25.6	0.164	0.124	32.3
	-60	0.174	0.157	10.8	0.131	0.111	18.0
	-75	0.139	0.145	-4.14	0.105	0.102	2.94
	-90	0.111	0.140	-20.7	0.0859	0.0987	-13.0

Table 11 Spherical blast wave diffraction over a convex corner as sketched in figure 18. Wall overpressure values, ΔP_w, are extracted from simulations at 5 mm height. Reference solutions are calculated from Kinney's law (1) and diffraction coefficients from [3] (see figure 5(b)). Errors are calculated with (39).